

N-Way Frequency Beamsplitter for Quantum Photonics

Richard Oliver,¹ Miri Blau,¹ Chaitali Joshi,^{1,*} Xingchen Ji,^{2,†}
Ricardo Gutiérrez-Jáuregui,^{3,4} Ana Asenjo-Garcia,³ Michal Lipson,^{1,2} and Alexander L. Gaeta^{1,2,‡}

¹*Department of Applied Physics and Applied Mathematics,
Columbia University, 500 W 120th St, New York, NY, 10027, US*

²*Department of Electrical Engineering, Columbia University, 500 W 120th St, New York, NY, 10027, US*

³*Department of Physics, Columbia University, 538 W 120th St, New York, NY, 10027, US*

⁴*Departamento de Física Cuántica y Fotónica, Instituto de Física,
Universidad Nacional Autónoma de México, Ciudad de México, 04510, México*

(Dated: May 16, 2024)

Optical networks are the leading platform for the transfer of information due to their low loss and ability to scale to many information channels using optical frequency modes. To fully leverage the quantum properties of light in this platform, it is desired to manipulate higher-dimensional superpositions by orchestrating linear, beamsplitter-type interactions between several channels simultaneously. We propose a method of achieving simultaneous, all-to-all coupling between N optical frequency modes via N -way Bragg-scattering four-wave mixing. By exploiting the frequency degree of freedom, additional modes can be multiplexed in an interaction medium of fixed volume and loss, avoiding the introduction of excess noise. We generalize the theory of the frequency-encoded two-mode interaction to N modes under this four-wave mixing approach and experimentally verify the quantum nature of this scheme by demonstrating three-way multiphoton interference. The two input photons are shared among three frequency modes and display interference differing from that of two classical (coherent-state) inputs. These results show the potential of our approach for the scalability of photonic quantum information processing to general N -mode systems in the frequency domain.

I. INTRODUCTION

Central to the viability of all quantum information platforms is the ability to scale the number information channels and their interactions without compromising performance. Regardless of physical implementation, scalability is critical for a wide variety of applications, including demonstrations of computational quantum advantage [1–4], fault tolerance [5, 6], quantum metrology and distributed sensing [7–10], and quantum communication [11–20].

In recent years, quantum photonic experiments have made progress towards scalability using both discrete [2, 21] and continuous variables [3, 4, 10, 22, 23], positioning photonic systems as a promising platform for quantum information processing. Light enjoys numerous advantages as an information carrier including low decoherence due to limited interactions with its environment. Nevertheless, nonlinear interactions between photons tend to be far weaker than linear ones, a fact which leans proposals for photonic quantum computing towards measurement-based models in which measurements effect nonlinear interactions [24, 25]. Whatever the computational viability of optical qubits, optical quantum networks are an ideal way of providing interconnections due to the low loss and dispersion of the telecom network, and optical interferometers will continue to serve as natural platforms for quantum metrology as they have throughout the history of the field. All of these applications make use of linear coupling between optical modes, conventionally achieved via sequential two-port beamsplitters. However, since such interactions are limited to coupling two modes at a time (e.g. polarization or spatial modes), additional losses are incurred with each added interaction, impeding scalability.

Interference between two frequency modes, in particular frequency-domain Hong-Ou-Mandel interference [26], has been proposed and experimentally established using both four-wave mixing and electro-optic approaches [27–31]. While frequency-domain interference beyond two modes has been treated both theoretically and experimentally using four-wave mixing in the classical regime [32, 33], as well as using electro-optic modulation in both classical and quantum regimes with single or parallel qudits [30, 33–40], frequency-domain interference of correlated photon pairs in more than two modes has not been shown.

We move beyond the two-mode limit by implementing N -way Bragg-scattering four-wave mixing (BS-FWM). This process coherently [41] interacts optical modes of different frequencies and can be viewed as a beamsplitter in the

* Present affiliation: Google Quantum AI, Santa Barbara, 93111, US.

† Present affiliation: John Hopcroft Center for Computer Science, School of Electronic Information and Electrical Engineering, Shanghai Jiao Tong University, Shanghai, 200240, China; State Key Lab of Advanced Optical Communication Systems and Networks, Department of Electronic Engineering, Shanghai Jiao Tong University, Shanghai, 200240, China

‡ Corresponding author: alg2207@columbia.edu

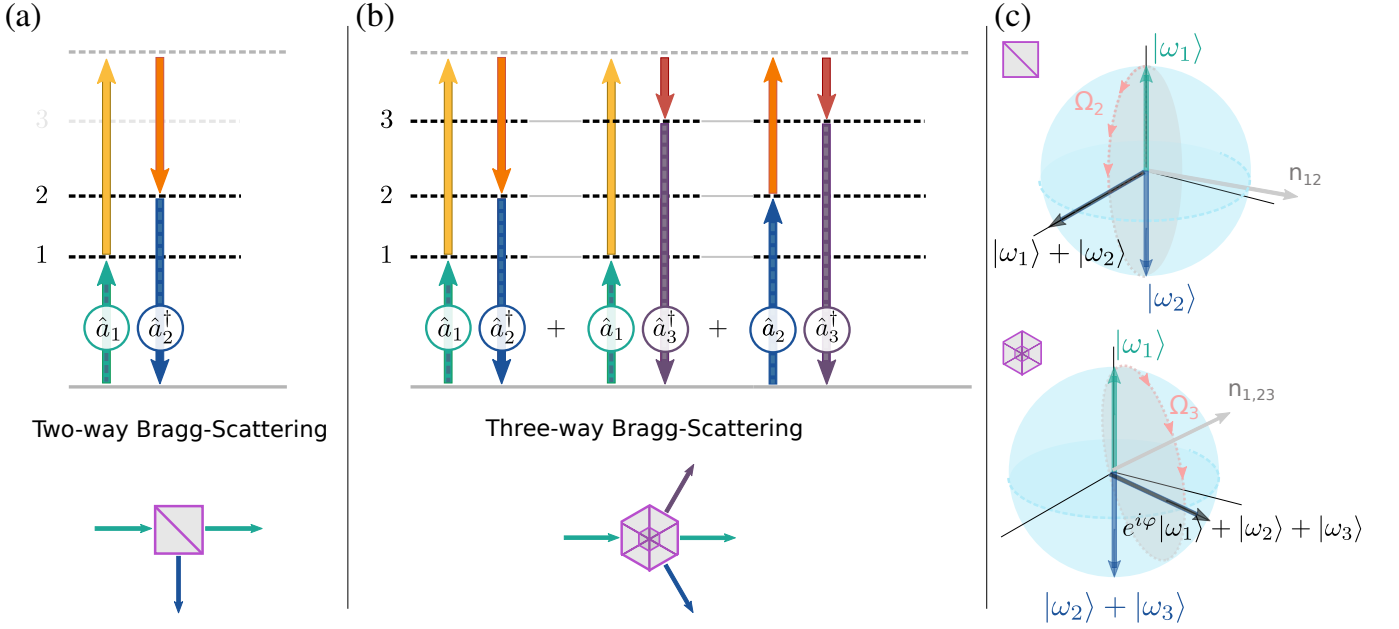


FIG. 1. Energy-level diagrams for the two-way (a) and three-way (b) Bragg-scattering four-wave mixing process (BS-FWM), where a photon (dashed arrows) is transferred from one mode to another with the aid of two pump beams (solid arrows) satisfying phase-matching conditions. This nonlinear, pairwise process is extended in (b) to occur simultaneously through three different channels. The process is coherent, allowing for excitations to be exchanged between the modes and can be understood in analogy to a frequency-domain beam-splitter (bottom panels). For simplicity the reverse creation/destruction processes are not shown. (c) When the modes share a single excitation, the coherent transfer is represented by the Bloch sphere, where the north pole represents the initial mode and the south pole represents either the second mode (two-way) or a superposition of the second and third modes (three-way).

frequency domain. Whereas conventional beamsplitters such as polarizing beamsplitters are limited to interfering two modes at a time, N -way BS-FWM couples all pairs among N modes selected from a continuum and multiplexed together, which enables control over a full bosonic N -level system (Fig. 1). We theoretically articulate the extension of the basic 2×2 Hamiltonian to an $N \times N$ one, demonstrating it experimentally for $N = 3$. Not only can this method extend the number of interacting modes and induce an all-to-all interaction, but it also has the advantage of allowing frequency conversion over hundreds of GHz, making it compatible with the frequency spacings of photons generated by existing small-footprint ($\sim 100 \mu\text{m}$ -radius) integrated microresonators. Optical multiport interferometers have been extensively studied [42, 43] with experimental realizations focusing particularly on spatial [44–50] and temporal [51–54] modes. Unlike the $\chi^{(2)}$ proposal for generating a frequency beamsplitter in [54], in our approach the sets of input and output frequency modes are identical. This ensures symmetric optics constraints on the input state as on the output and readily allows for incorporation within existing optical networks designed for fixed frequency grids within a single optical band.

Bragg-scattering four-wave mixing (BS-FWM) is a noiseless, nonlinear process capable of performing unitary transformations between two optical frequency modes interacting in a third-order ($\chi^{(3)}$) nonlinear medium (Fig. 1) [27, 55–63]. Since a nonlinear fiber is capable of extremely low propagation losses ($< 1\%$ for the 100-m length of fiber in this experiment), deviations from unitary, noiseless operation are minute. This frequency-conversion process is depicted in Fig. 1a, where two high-intensity pump fields (solid yellow and orange) induce the coherent transfer of population between two frequency modes, traditionally termed the signal and idler (dashed green and blue). In the frequency domain, this process is identical to a beamsplitter, for which the input and output ports correspond to frequency channels. In the case of a single-photon excitation, the signal/idler frequency modes constitute a two-level system, and the four-wave-mixing interaction is equivalent to a rotation on the Bloch sphere in which the poles represent the two modes while all other points correspond to coherent superpositions [41]. An efficient population transfer must satisfy energy and momentum conservation, known as phase-matching. By simultaneously phase-matching multiple processes we can realize a three-way frequency beamsplitter, represented graphically in Fig. 1b. Alternatively, this may be viewed as a transformation on a three-level system, without adding noise or loss.

II. THEORY

The theory of BS-FWM among N modes can be developed from the two-mode case. The dynamics of Bragg scattering between two frequency modes is given by the spatial propagation Hamiltonian, $\hat{H}_{N=2} = 2\gamma A_1 A_2^* \hat{a}_1 \hat{a}_2^\dagger + H.a.$, along with the spatial Heisenberg equations [56] for a given operator \hat{O} , $d\hat{O}/dz = i[\hat{O}, \hat{H}]$. In this Hamiltonian, A_i represents the complex amplitude of the i^{th} pump field (units of $\text{W}^{1/2}$), γ is the effective nonlinearity ($\text{W}^{-1}\text{m}^{-1}$), and $\hat{a}_i(z)$ is the bosonic operator annihilating the i^{th} frequency mode at the position z as it propagates along the fiber. The operators \hat{a}_i obey equal-position commutation relations $[\hat{a}_i(z), \hat{a}_j^\dagger(z)] = \delta_{ij}$. The Heisenberg-picture dynamics for the above Hamiltonian induce the following relationship between the input and output fields, where L is the length of the nonlinear medium:

$$\begin{bmatrix} \hat{a}_1(L) \\ \hat{a}_2(L) \end{bmatrix} = \exp \left\{ iL \begin{bmatrix} 0 & 2\gamma A_1^* A_2 \\ 2\gamma A_1 A_2^* & 0 \end{bmatrix} \right\} \begin{bmatrix} \hat{a}_1(0) \\ \hat{a}_2(0) \end{bmatrix}. \quad (1)$$

The above process describes a matrix transformation of the input signal and idler fields, \hat{a}_i and is equivalent to a beamsplitter with input ports corresponding to the two input frequencies [27, 57]. Since the pumps are in a high-intensity coherent state, quantum features from the pumps are negligible so that the pump fields are represented as classical numbers.

The two-input case can be extended to that of N fields interacting via BS-FWM through the following Hamiltonian:

$$\hat{H}_N = \sum_{i \neq j} 2\gamma A_i A_j^* \hat{a}_i \hat{a}_j^\dagger. \quad (2)$$

Note that although the effective nonlinearity γ is wavelength-dependent, in this equation it corresponds to the carrier wavelength and is therefore treated as a constant of the fiber. As in the case of two modes, the Heisenberg equations of motion yield an $SU(N)$ transformation between the N interacting fields such that,

$$\begin{bmatrix} \hat{a}_1(L) \\ \vdots \\ \hat{a}_N(L) \end{bmatrix} = \exp \left\{ iL \begin{bmatrix} 0 & & 2\gamma A_i^* A_j \\ & \ddots & \\ 2\gamma A_i A_j^* & & 0 \end{bmatrix} \right\} \begin{bmatrix} \hat{a}_1(0) \\ \vdots \\ \hat{a}_N(0) \end{bmatrix}. \quad (3)$$

The inclusion of phase-matching introduces real diagonal elements in the above matrix (see Supplementary Material), which may be neglected in our experiment by suitable choice of wavelengths. Since the phase-matching condition and interaction strength of one pair (say between modes one and three) are determined by the phase-matching condition of the other two pairs (one-two and two-three), there is a limitation to the set of available transformations. This can also be seen from the observation that the number of degrees of freedom in the transformation matrix of Eq. 3 is $\mathcal{O}(N)$, whereas an arbitrary $SU(N)$ transformation is parametrized by $\mathcal{O}(N^2)$ numbers.

For the case of $N = 3$ pumps, assuming negligible phase mismatch and equal pump powers $|A_i| = P$, the transformation may be written as a function of nonlinear phase $\phi = 2\gamma LP$ (see Supplementary Material):

$$\begin{bmatrix} \hat{a}_1(L) \\ \hat{a}_2(L) \\ \hat{a}_3(L) \end{bmatrix} = \begin{bmatrix} p(\phi) & q(\phi) & q(\phi) \\ q(\phi) & p(\phi) & q(\phi) \\ q(\phi) & q(\phi) & p(\phi) \end{bmatrix} \begin{bmatrix} \hat{a}_1(0) \\ \hat{a}_2(0) \\ \hat{a}_3(0) \end{bmatrix}, \quad (4)$$

where $q(\phi) = (e^{3i\phi} - 1)/3$, $p(\phi) = q(\phi) + 1$.

Whereas a polarizing beamsplitter is restricted to two input ports, we demonstrate that a frequency-domain beamsplitter may couple more than two modes within the same nonlinear medium. A frequency-domain beamsplitter therefore scales favorably with respect to loss and complexity in comparison with concatenating spatial-mode beamsplitters for N -mode operation since additional ports can be multiplexed in the same waveguide, keeping propagation loss fixed in a single device with the same physical size [64].

To demonstrate the all-to-all interaction, we consider both attenuated coherent states as well as photons as inputs. For a single-frequency input in mode one, the populations in the three frequency modes are given by $\langle \hat{a}_1^\dagger \hat{a}_1 \rangle = |p(\phi)|^2$, $\langle \hat{a}_2^\dagger \hat{a}_2 \rangle = \langle \hat{a}_3^\dagger \hat{a}_3 \rangle = |q(\phi)|^2$. Experimentally, these correspond to single-click detection events (“singles rates”). These expressions hold for both coherent states and single photons and represent tunable transmission coefficients of a three-way beamsplitter.

Extending to dual-frequency inputs, in which modes one and three are excited, we now compute both the first- and second-order correlation functions corresponding to either two attenuated coherent states or a photon pair. The analytical results for both correlation functions (singles and coincidences) are tabulated in Table I and assume equal intensities of each input channel (in addition to the assumptions behind Eq. 4). The first-order correlation functions (singles counts) are identical; only in the second-order correlation functions or coincidences are non-classical statistics revealed. The coherent states yield uncorrelated or accidental coincidences given by the product of their singles counts, whereas correlated photon pairs show genuine two-photon interference, an extension of the Hong-Ou-Mandel effect.

TABLE I. Theoretical detection statistics of the dual-frequency state after Bragg scattering, corresponding to first- and second-order correlation functions. Note that by the symmetry of the inputs $\langle \hat{a}_1^\dagger \hat{a}_1 \rangle = \langle \hat{a}_3^\dagger \hat{a}_3 \rangle$ and $\langle \hat{a}_1^\dagger \hat{a}_2^\dagger \hat{a}_2 \hat{a}_1 \rangle = \langle \hat{a}_2^\dagger \hat{a}_3^\dagger \hat{a}_3 \hat{a}_2 \rangle$.

	Dual-Freq. Coherent State Photon Pairs	
Singles	$\langle \hat{a}_1^\dagger \hat{a}_1 \rangle = 1 - q(\phi) ^2$	$\langle \hat{a}_1^\dagger \hat{a}_1 \rangle = 1 - q(\phi) ^2$
	$\langle \hat{a}_2^\dagger \hat{a}_2 \rangle = 2 q(\phi) ^2$	$\langle \hat{a}_2^\dagger \hat{a}_2 \rangle = 2 q(\phi) ^2$
Coincidences	$\langle \hat{a}_i^\dagger \hat{a}_j^\dagger \hat{a}_j \hat{a}_i \rangle = \langle \hat{a}_i^\dagger \hat{a}_i \rangle \langle \hat{a}_j^\dagger \hat{a}_j \rangle$	$\langle \hat{a}_1^\dagger \hat{a}_2^\dagger \hat{a}_2 \hat{a}_1 \rangle = p(\phi)q(\phi) + q^2(\phi) ^2$
		$\langle \hat{a}_1^\dagger \hat{a}_3^\dagger \hat{a}_3 \hat{a}_1 \rangle = p^2(\phi) + q^2(\phi) ^2$

III. RESULTS

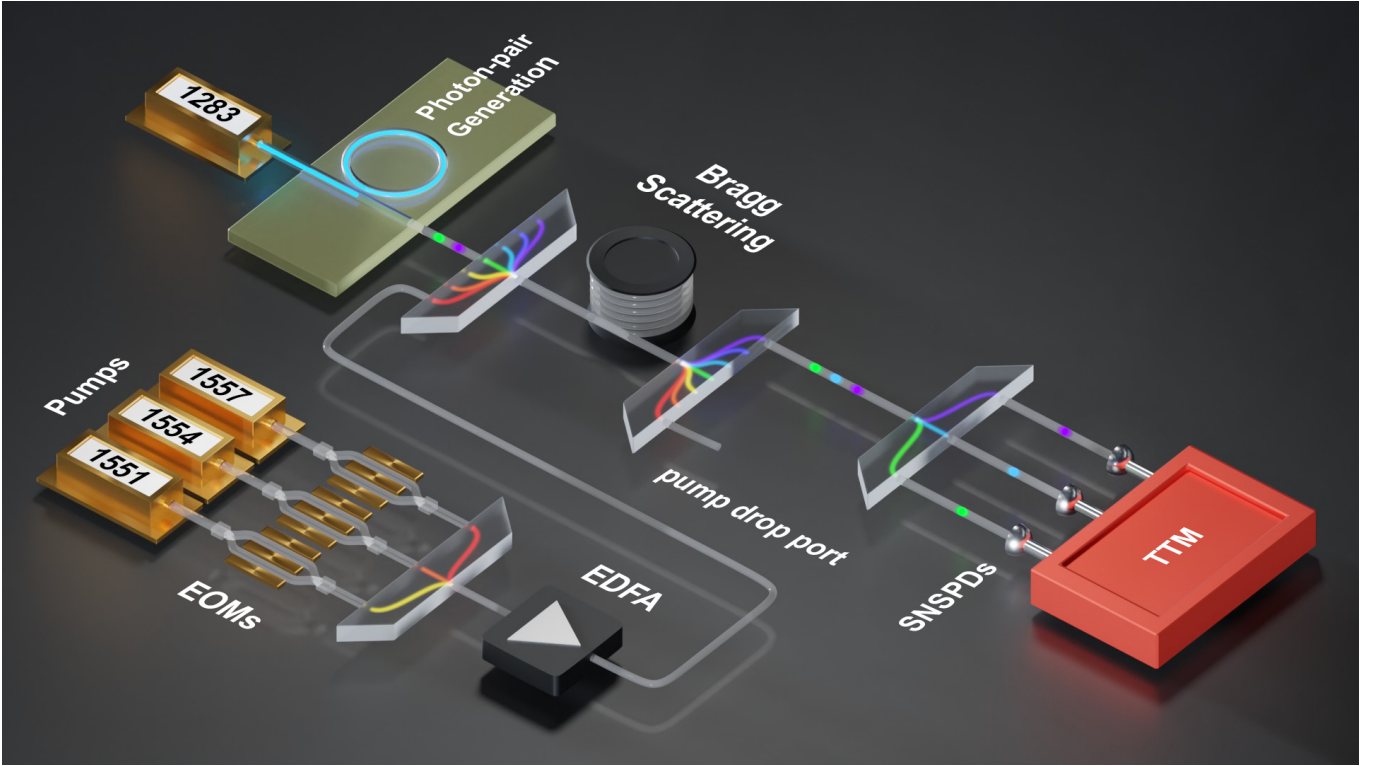


FIG. 2. Three-Way Bragg-Scattering Four-Wave Mixing. Two photons are sent into two of the three frequency ports of the nonlinear fiber. Before the fiber they are wavelength-multiplexed with the three Bragg pumps, shown at bottom left being modulated and then amplified to generate high-peak-power pulses. Following the fiber the pumps are filtered out of the system and the photons generated at the three output channels are filtered and sent to their respective detectors. EOM, electro-optic modulator; EDFA, erbium-doped fiber amplifier; SNSPD, superconducting nanowire single-photon detector; TTM, time-tagging module.

We experimentally demonstrate a three-way interaction via Bragg-scattering FWM to realize all-to-all coupling in the three-mode system. Fig. 2 shows our experimental setup with three frequency modes in the O-band (1260-1360 nm). Our correlated photon pairs are generated through spontaneous four-wave mixing (SFWM) in a SiN

microresonator. The microresonator is pumped with a CW laser at 1282.8 nm, and the generated photons are combined with the three strong classical pump fields located in the C band (1530-1565 nm) and sent to a dispersion-shifted fiber (Corning Vistacor) for a nearly perfectly phase-matched nonlinear interaction (see Fig. 2). The powers of the classical pumps are scanned to obtain the nonlinear-phase-dependent interference pattern (Figs. 3, 4). After the nonlinear interaction, the three frequency arms are separated, filtered, and detected with superconducting nanowire single photon detectors synchronized with a time tagging module for coincidence counting.

We begin by exciting our system in the classical regime by injecting a single-wavelength weak coherent state and measuring the energy exchange between the three frequency modes while varying the nonlinear phase ϕ_{NL} . As the nonlinear phase increases, the input signal is converted to the other wavelength channels (see Fig. 3a). For a nonlinear phase of $\phi_{NL} = 2\pi/9$, power in the input signal is shared evenly between all three frequency modes, equivalent to a frequency-domain tritter [30]. The measured spectrum confirms that Bragg scattering is limited to the three channels of interest. Further, the spectrum confirms that power from the input signal is symmetrically distributed between the other channels. Note that the difference in spectral peak heights is due to the pulsing of the BS-FWM process, so that the generated idlers are pulses with a duty cycle of 26.2 dB. The additional contribution to peak height is the relative generation rate factor (compared to CW input) of approximately one third. The spectrum is thus essential in confirming these properties of our three-way nonlinear process.

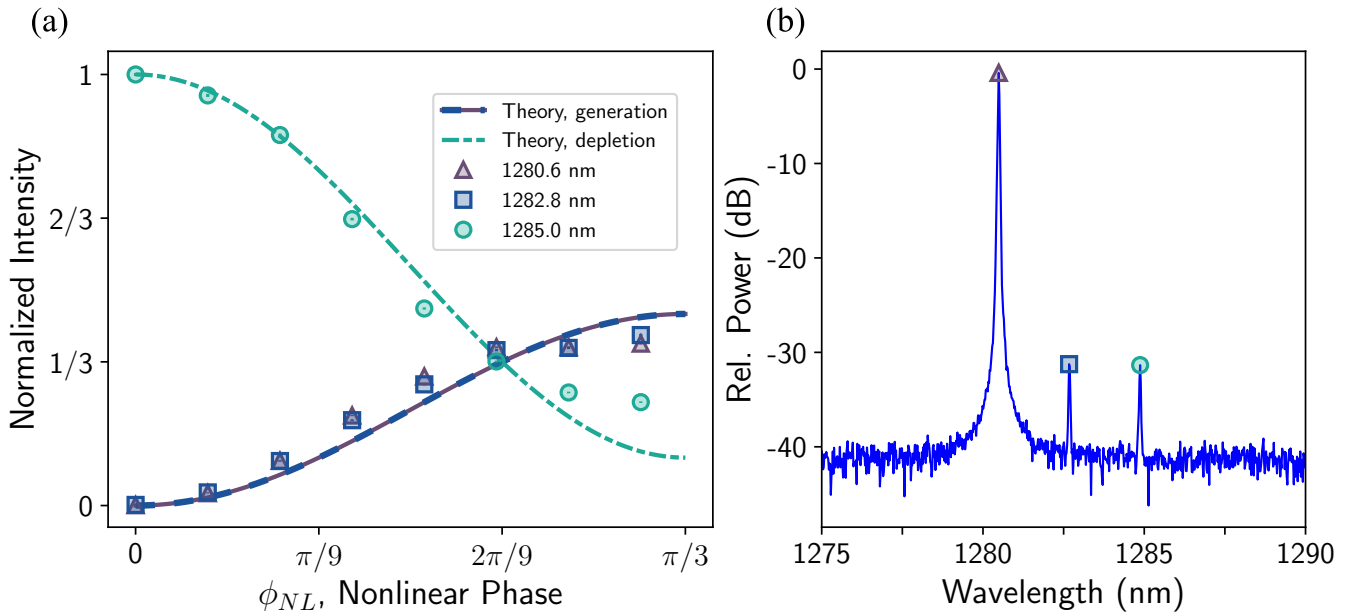


FIG. 3. (a) Normalized rates of single-click events as a function of the nonlinear phase ϕ_{NL} . The classical input (here an attenuated coherent state at 1285.0 nm) is converted to the other two signals (at 1280.6 nm, purple, and 1282.8 nm, blue). (b) Optical spectrum of the output fields after a nonlinear interaction such that the three frequency modes share nearly equal power, corresponding to $\phi_{NL} = 2\pi/9$. The difference in average power level between the continuous-wave input (here 1280.6 nm) and the outputs at the converted frequencies (1282.8 nm, 1285.0 nm) corresponds to the duty cycle of the pump pulses and therefore that of the newly generated output pulses. The all-to-all interaction is controlled by using phase-matching to confine the coupling to the three frequencies shown; coupling to external frequency modes is negligible.

Observable differences arise between the statistics of coherent states and single-photon states. Whereas the above first-order interferences do not discern classical weak coherent states from photon pairs, the second-order correlation measurements do distinguish these inputs, which we illustrate by performing integrated $g^{(2)}$ measurements, shown in Fig. 4 for each type of input state. The coincidence rates of the weak coherent state are given by the square of the singles rates, as expected for a correlation of two independent variables. Meanwhile, the coincidence rates for the photon-pair input notably decrease faster as a function of nonlinear phase. This feature may be interpreted as an extension to the three-mode system of Hong-Ou-Mandel interference, in which coincidences vanish at the nonlinear phase corresponding to a 50:50 beamsplitter [31]. The interference curve is lifted further by the nonzero multi-photon component simultaneously with the asymmetric loss on each frequency channel following pair generation and prior to interference, as predicted by theory in the Supplementary Material. After carefully accounting for these effects, we observe excellent agreement with theory.

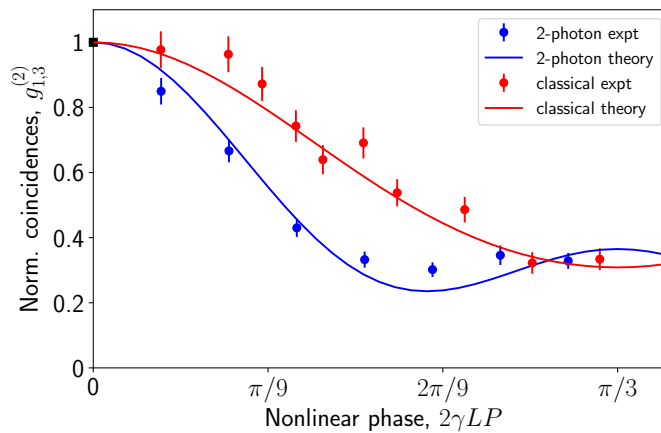


FIG. 4. Measured coincidences (integrated $g^{(2)}$ normalized to rates at zero nonlinear phase) for photon pairs (blue) versus two classical, attenuated coherent states (red) after N-way BSFWM.

IV. DISCUSSION

We propose an all-to-all coherent photonic interaction between N frequency modes and experimentally demonstrate the system for three modes. The coupling is low-noise and allows for coherent transfer of population between the modes. The available unitary transformations in our scheme are dictated by phase-matching considerations. Phase-matching is a momentum conservation phenomenon, and as such, requires careful dispersion engineering to tailor the desired transformations. In our case, the phase-matching conditions are constrained by higher-order dispersion. In the case we realize here, we phase-match all three pairs of frequency modes.

To practically scale beyond three modes, it is possible to take advantage of the higher-order phase-matching such that each pair of modes may be coupled by a unique pair of pumps. This places only a classical overhead on the system, to be expected from the fundamental requirements for an $N \times N$ transformation. Most importantly, adding to the number of pumps allows for scaling the number of beamsplitters without introducing additional losses. Further, owing to the fact that Bragg-scattering can couple optical modes separated by 100s of GHz, our scheme is compatible with typical resonance spacings of integrated microresonator-based quantum sources, as shown in this experiment. As BSFWM has already been demonstrated in an integrated platform (including suitability for use with quantum states) [60, 61, 63], we envision full integration of quantum state generation and manipulation using our scheme.

Our measurements represent the first demonstration of two-photon interference across more than two modes in the frequency domain using N-way BS-FWM. We show theoretically how interfering N modes is possible using the same number of pump modes, opening the door to a demonstration of quantum advantage via frequency-domain boson sampling. This work therefore represents a pathway towards scalability of photonic quantum information processing in the frequency domain.

This research was supported in part by the National Science Foundation (OMA-1936345, PHY-2110615) and the Department of Energy, Office of Science, National Quantum Information Science Research Centers, Co-design Center for Quantum Advantage (C²QA).

-
- [1] Frank Arute, Kunal Arya, Ryan Babbush, Dave Bacon, Joseph C. Bardin, Rami Barends, Rupak Biswas, Sergio Boixo, Fernando G. S. L. Brandao, David A. Buell, Brian Burkett, Yu Chen, Zijun Chen, Ben Chiaro, Roberto Collins, William Courtney, Andrew Dunsworth, Edward Farhi, Brooks Foxen, Austin Fowler, Craig Gidney, Marissa Giustina, Rob Graff, Keith Guerin, Steve Habegger, Matthew P. Harrigan, Michael J. Hartmann, Alan Ho, Markus Hoffmann, Trent Huang, Travis S. Humble, Sergei V. Isakov, Evan Jeffrey, Zhang Jiang, Dvir Kafri, Kostyantyn Kechedzhi, Julian Kelly, Paul V. Klimov, Sergey Knysh, Alexander Korotkov, Fedor Kostritsa, David Landhuis, Mike Lindmark, Erik Lucero, Dmitry Lyakh, Salvatore Mandra, Jarrod R. McClean, Matthew McEwen, Anthony Megrant, Xiao Mi, Kristel Michielsen, Masoud Mohseni, Josh Mutus, Ofer Naaman, Matthew Neeley, Charles Neill, Murphy Yuezhen Niu, Eric Ostby, Andre Petukhov, John C. Platt, Chris Quintana, Eleanor G. Rieffel, Pedram Roushan, Nicholas C. Rubin, Daniel Sank, Kevin J. Satzinger, Vadim Smelyanskiy, Kevin J. Sung, Matthew D. Trevithick, Amit Vainsencher, Benjamin Villalonga, Theodore

- White, Z. Jamie Yao, Ping Yeh, Adam Zalcman, Hartmut Neven, and John M. Martinis. Quantum supremacy using a programmable superconducting processor. *Nature*, 574(7779):505–510, Oct 2019.
- [2] Hui Wang, Jian Qin, Xing Ding, Ming-Cheng Chen, Si Chen, Xiang You, Yu-Ming He, Xiao Jiang, L. You, Z. Wang, C. Schneider, Jelmer J. Renema, Sven Höfling, Chao-Yang Lu, and Jian-Wei Pan. Boson sampling with 20 input photons and a 60-mode interferometer in a 10^{14} -dimensional hilbert space. *Phys. Rev. Lett.*, 123:250503, Dec 2019.
 - [3] Han-Sen Zhong, Hui Wang, Yu-Hao Deng, Ming-Cheng Chen, Li-Chao Peng, Yi-Han Luo, Jian Qin, Dian Wu, Xing Ding, Yi Hu, Peng Hu, Xiao-Yan Yang, Wei-Jun Zhang, Hao Li, Yuxuan Li, Xiao Jiang, Lin Gan, Guangwen Yang, Lixing You, Zhen Wang, Li Li, Nai-Le Liu, Chao-Yang Lu, and Jian-Wei Pan. Quantum computational advantage using photons. *Science*, 370(6523):1460–1463, 2020.
 - [4] Lars S. Madsen, Fabian Laudenbach, Mohsen Falamarzi Askarani, Fabien Rortais, Trevor Vincent, Jacob F. F. Bulmer, Filippo M. Miatto, Leonhard Neuhaus, Lukas G. Helt, Matthew J. Collins, Adriana E. Lita, Thomas Gerrits, Sae Woo Nam, Varun D. Vaidya, Matteo Menotti, Ish Dhand, Zachary Vernon, Nicolás Quesada, and Jonathan Lavoie. Quantum computational advantage with a programmable photonic processor. *Nature*, 606(7912):75–81, June 2022. Number: 7912 Publisher: Nature Publishing Group.
 - [5] Austin G. Fowler, Matteo Mariantoni, John M. Martinis, and Andrew N. Cleland. Surface codes: Towards practical large-scale quantum computation. *Physical Review A*, 86(3):032324, September 2012.
 - [6] Rajeev Acharya, Igor Aleiner, Richard Allen, Trond I. Andersen, Markus Ansmann, Frank Arute, Kunal Arya, Abraham Asfaw, Juan Atalaya, Ryan Babbush, Dave Bacon, Joseph C. Bardin, Joao Basso, Andreas Bengtsson, Sergio Boixo, Gina Bortoli, Alexandre Bourassa, Jenna Bovaird, Leon Brill, Michael Broughton, Bob B. Buckley, David A. Buell, Tim Burger, Brian Burkett, Nicholas Bushnell, Yu Chen, Zijun Chen, Ben Chiaro, Josh Cogan, Roberto Collins, Paul Conner, William Courtney, Alexander L. Crook, Ben Curtin, Dripto M. Debroy, Alexander Del Toro Barba, Sean Demura, Andrew Dunsworth, Daniel Eppens, Catherine Erickson, Lara Faoro, Edward Farhi, Reza Fatemi, Leslie Flores Burgos, Ebrahim Forati, Austin G. Fowler, Brooks Foxen, William Giang, Craig Gidney, Dar Gilboa, Marissa Giustina, Alejandro Grajales Dau, Jonathan A. Gross, Steve Habegger, Michael C. Hamilton, Matthew P. Harrigan, Sean D. Harrington, Oscar Higgott, Jeremy Hilton, Markus Hoffmann, Sabrina Hong, Trent Huang, Ashley Huff, William J. Huggins, Lev B. Ioffe, Sergei V. Isakov, Justin Iveland, Evan Jeffrey, Zhang Jiang, Cody Jones, Pavol Juhas, Dvir Kafri, Kostyantyn Kechedzhi, Julian Kelly, Tanuj Khatkar, Mostafa Khezri, Mária Kieferová, Seon Kim, Alexei Kitaev, Paul V. Klimov, Andrey R. Klots, Alexander N. Korotkov, Fedor Kostritsa, John Mark Kreikebaum, David Landhuis, Pavel Laptev, Kim-Ming Lau, Lily Laws, Joonho Lee, Kenny Lee, Brian J. Lester, Alexander Lill, Wayne Liu, Aditya Locharla, Erik Lucero, Fionn D. Malone, Jeffrey Marshall, Orion Martin, Jarrod R. McClean, Trevor McCourt, Matt McEwen, Anthony Megrant, Bernardo Meurer Costa, Xiao Mi, Kevin C. Miao, Masoud Mohseni, Shirin Montazeri, Alexis Morvan, Emily Mount, Wojciech Mruczkiewicz, Ofer Naaman, Matthew Neeley, Charles Neill, Ani Nersisyan, Hartmut Neven, Michael Newman, Jiun How Ng, Anthony Nguyen, Murray Nguyen, Murphy Yuezhen Niu, Thomas E. O’Brien, Alex Opremcak, John Platt, Andre Petukhov, Rebecca Potter, Leonid P. Pryadko, Chris Quintana, Pedram Roushan, Nicholas C. Rubin, Negar Saei, Daniel Sank, Kannan Sankaragomathi, Kevin J. Satzinger, Henry F. Schurkus, Christopher Schuster, Michael J. Shearn, Aaron Shorter, Vladimir Shvarts, Jindra Skrzny, Vadim Smelyanskiy, W. Clarke Smith, George Sterling, Doug Strain, Marco Szalay, Alfredo Torres, Guifre Vidal, Benjamin Villalonga, Catherine Vollgraf Heidweiller, Theodore White, Cheng Xing, Z. Jamie Yao, Ping Yeh, Juhwan Yoo, Grayson Young, Adam Zalcman, Yaxing Zhang, Ningfeng Zhu, and Google Quantum AI. Suppressing quantum errors by scaling a surface code logical qubit. *Nature*, 614(7949):676–681, February 2023.
 - [7] Vittorio Giovannetti, Seth Lloyd, and Lorenzo Maccone. Quantum metrology. *Phys. Rev. Lett.*, 96:010401, Jan 2006.
 - [8] Vittorio Giovannetti, Seth Lloyd, and Lorenzo Maccone. Advances in quantum metrology. *Nature Photonics*, 5(4):222–229, April 2011. Number: 4 Publisher: Nature Publishing Group.
 - [9] Wenchao Ge, Kurt Jacobs, Zachary Eldredge, Alexey V. Gorshkov, and Michael Foss-Feig. Distributed Quantum Metrology with Linear Networks and Separable Inputs. *Physical Review Letters*, 121(4):043604, July 2018.
 - [10] Quntao Zhuang, Zheshe Zhang, and Jeffrey H. Shapiro. Distributed quantum sensing using continuous-variable multipartite entanglement. *Physical Review A*, 97(3):032329, March 2018.
 - [11] H. Bechmann-Pasquinucci and W. Tittel. Quantum cryptography using larger alphabets. *Phys. Rev. A*, 61:062308, May 2000.
 - [12] Nicolas J. Cerf, Mohamed Bourennane, Anders Karlsson, and Nicolas Gisin. Security of quantum key distribution using d -level systems. *Phys. Rev. Lett.*, 88:127902, Mar 2002.
 - [13] Simon Gröblacher, Thomas Jennewein, Alipasha Vaziri, Gregor Weihs, and Anton Zeilinger. Experimental quantum cryptography with qutrits. *New Journal of Physics*, 8(5):75, may 2006.
 - [14] Lana Sheridan and Valerio Scarani. Security proof for quantum key distribution using qudit systems. *Physical Review A*, 82(3):030301, September 2010. Publisher: American Physical Society.
 - [15] Mohammad Mirhosseini, Omar S Magaña-Loaiza, Malcolm N O’Sullivan, Brandon Rodenburg, Mehul Malik, Martin P J Lavery, Miles J Padgett, Daniel J Gauthier, and Robert W Boyd. High-dimensional quantum cryptography with twisted light. *New Journal of Physics*, 17(3):033033, mar 2015.
 - [16] Irfan Ali-Khan, Curtis J. Broadbent, and John C. Howell. Large-Alphabet Quantum Key Distribution Using Energy-Time Entangled Bipartite States. *Physical Review Letters*, 98(6):060503, February 2007. Publisher: American Physical Society.
 - [17] Nurul T. Islam, Charles Ci Wen Lim, Clinton Cahall, Jungsang Kim, and Daniel J. Gauthier. Provably secure and high-rate quantum key distribution with time-bin qudits. *Science Advances*, 3(11):e1701491, 2017.
 - [18] Catherine Lee, Darius Bunandar, Zheshe Zhang, Gregory R. Steinbrecher, P. Ben Dixon, Franco N. C. Wong, Jeffrey H. Shapiro, Scott A. Hamilton, and Dirk Englund. Large-alphabet encoding for higher-rate quantum key distribution. *Optics*

Express, 27(13):17539, June 2019.

- [19] Xiao-Min Hu, Yu Guo, Bi-Heng Liu, Yun-Feng Huang, Chuan-Feng Li, and Guang-Can Guo. Beating the channel capacity limit for superdense coding with entangled ququarts. *Science Advances*, 4(7), July 2018.
- [20] Daniele Cozzolino, Beatrice Da Lio, Davide Bacco, and Leif Katsuo Oxenløwe. High-Dimensional Quantum Communication: Benefits, Progress, and Future Challenges. *Advanced Quantum Technologies*, 2(12):1900038, 2019.
- [21] Sara Bartolucci, Patrick Birchall, Hector Bombín, Hugo Cable, Chris Dawson, Mercedes Gimeno-Segovia, Eric Johnston, Konrad Kieling, Naomi Nickerson, Mihir Pant, Fernando Pastawski, Terry Rudolph, and Chris Sparrow. Fusion-based quantum computation. *Nature Communications*, 14(1):912, February 2023. Number: 1 Publisher: Nature Publishing Group.
- [22] Mikkel V. Larsen, Xueshi Guo, Casper R. Breum, Jonas S. Neergaard-Nielsen, and Ulrik L. Andersen. Deterministic generation of a two-dimensional cluster state. *Science*, 366(6463):369–372, 2019.
- [23] Shota Yokoyama, Ryuji Ukai, Seiji C. Armstrong, Chanond Sornphiphatphong, Toshiyuki Kaji, Shigenari Suzuki, Jun-ichi Yoshikawa, Hidehiro Yonezawa, Nicolas C. Menicucci, and Akira Furusawa. Ultra-large-scale continuous-variable cluster states multiplexed in the time domain. *Nature Photonics*, 7(12), December 2013.
- [24] E. Knill, R. Laflamme, and G. J. Milburn. A scheme for efficient quantum computation with linear optics. *Nature*, 409(6816):46–52, January 2001. Number: 6816 Publisher: Nature Publishing Group.
- [25] Robert Raussendorf and Hans J. Briegel. A One-Way Quantum Computer. *Physical Review Letters*, 86(22):5188–5191, May 2001.
- [26] C. K. Hong, Z. Y. Ou, and L. Mandel. Measurement of subpicosecond time intervals between two photons by interference. *Phys. Rev. Lett.*, 59:2044–2046, Nov 1987.
- [27] M. G. Raymer, S. J. van Enk, C. J. McKinstrie, and H. J. McGuinness. Interference of two photons of different color. *Optics Communications*, 283(5):747–752, March 2010.
- [28] Toshiaki Kobayashi, Rikizo Ikuta, Shuto Yasui, Shigehito Miki, Taro Yamashita, Hirotaka Terai, Takashi Yamamoto, Masato Koashi, and Nobuyuki Imoto. Frequency-domain Hong–Ou–Mandel interference. *Nature Photonics*, 10(7):441–444, July 2016.
- [29] Poolad Imany, Ogaga D. Odele, Mohammed S. Alshaykh, Hsuan-Hao Lu, Daniel E. Leaird, and Andrew M. Weiner. Frequency-domain Hong–Ou–Mandel interference with linear optics. *Optics Letters*, 43(12):2760, June 2018.
- [30] Hsuan-Hao Lu, Joseph M. Lukens, Nicholas A. Peters, Ogaga D. Odele, Daniel E. Leaird, Andrew M. Weiner, and Pavel Lougovski. Electro-Optic Frequency Beam Splitters and Titters for High-Fidelity Photonic Quantum Information Processing. *Physical Review Letters*, 120(3):030502, January 2018.
- [31] Chaitali Joshi, Alessandro Farsi, Avik Dutt, Bok Young Kim, Xingchen Ji, Yun Zhao, Andrew M. Bishop, Michal Lipson, and Alexander L. Gaeta. Frequency-Domain Quantum Interference with Correlated Photons from an Integrated Microresonator. *Physical Review Letters*, 124(14):143601, April 2020. Publisher: American Physical Society.
- [32] Bryn A. Bell, Kai Wang, Alexander S. Solntsev, Dragomir N. Neshev, Andrey A. Sukhorukov, and Benjamin J. Eggleton. Spectral photonic lattices with complex long-range coupling. *Optica*, 4(11):1433–1436, November 2017. Publisher: Optical Society of America.
- [33] Kai Wang, Bryn A. Bell, Alexander S. Solntsev, Dragomir N. Neshev, Benjamin J. Eggleton, and Andrey A. Sukhorukov. Multidimensional synthetic chiral-tube lattices via nonlinear frequency conversion. *Light: Science & Applications*, 9(1):132, July 2020. Number: 1 Publisher: Nature Publishing Group.
- [34] Luqi Yuan, Yu Shi, and Shanhui Fan. Photonic gauge potential in a system with a synthetic frequency dimension. *Optics Letters*, 41(4):741, February 2016.
- [35] Yaowen Hu, Christian Reimer, Amirhassan Shams-Ansari, Mian Zhang, and Marko Loncar. Realization of high-dimensional frequency crystals in electro-optic microcombs. *Optica*, 7(9):1189, September 2020.
- [36] Yaowen Hu, Mengjie Yu, Di Zhu, Neil Sinclair, Amirhassan Shams-Ansari, Linbo Shao, Jeffrey Holzgrafe, Eric Puma, Mian Zhang, and Marko Loncar. On-chip electro-optic frequency shifters and beam splitters. *Nature*, 599(7886):587–593, November 2021. Publisher: Nature Publishing Group.
- [37] Siddharth Buddhiraju, Avik Dutt, Momchil Minkov, Ian A. D. Williamson, and Shanhui Fan. Arbitrary linear transformations for photons in the frequency synthetic dimension. *Nature Communications*, 12(1):2401, April 2021. Number: 1 Publisher: Nature Publishing Group.
- [38] Luqi Yuan, Avik Dutt, and Shanhui Fan. Synthetic frequency dimensions in dynamically modulated ring resonators. *APL Photonics*, 6(7):071102, July 2021.
- [39] Hsuan-Hao Lu, Hsuan-Hao Lu, Navin B. Lingaraju, Navin B. Lingaraju, Daniel E. Leaird, Andrew M. Weiner, and Joseph M. Lukens. High-dimensional discrete Fourier transform gates with a quantum frequency processor. *Optics Express*, 30(6):10126–10134, March 2022. Publisher: Optica Publishing Group.
- [40] Hsuan-Hao Lu, Karthik V. Myilswamy, Ryan S. Bennink, Suparna Seshadri, Mohammed S. Alshaykh, Junqiu Liu, Tobias J. Kippenberg, Daniel E. Leaird, Andrew M. Weiner, and Joseph M. Lukens. Bayesian tomography of high-dimensional on-chip biphoton frequency combs with randomized measurements. *Nature Communications*, 13(1):4338, July 2022. Number: 1 Publisher: Nature Publishing Group.
- [41] Stéphane Clemmen, Alessandro Farsi, Sven Ramelow, and Alexander L. Gaeta. Ramsey Interference with Single Photons. *Physical Review Letters*, 117(22):223601, November 2016.
- [42] Marek Zukowski, Anton Zeilinger, and Michael A. Horne. Realizable higher-dimensional two-particle entanglements via multiport beam splitters. *Physical Review A*, 55(4):2564–2579, April 1997.
- [43] Malte Christopher Tichy, Markus Tiersch, Fernando de Melo, Florian Mintert, and Andreas Buchleitner. Zero-Transmission Law for Multiport Beam Splitters. *Physical Review Letters*, 104(22):220405, June 2010.

- [44] Gregor Weihs, Michael Reck, Harald Weinfurter, and Anton Zeilinger. Two-photon interference in optical fiber multiports. *Physical Review A*, 54(1):893–897, July 1996.
- [45] Nicolò Spagnolo, Lorenzo Aparo, Chiara Vitelli, Andrea Crespi, Roberta Ramponi, Roberto Osellame, Paolo Mataloni, and Fabio Sciarrino. Quantum interferometry with three-dimensional geometry. *Scientific Reports*, 2(1):862, November 2012. Number: 1 Publisher: Nature Publishing Group.
- [46] Thomas Meany, Michael Delanty, Simon Gross, Graham D. Marshall, M. J. Steel, and Michael J. Withford. Non-classical interference in integrated 3D multiports. *Optics Express*, 20(24):26895–26905, November 2012. Publisher: Optica Publishing Group.
- [47] Andrea Crespi, Roberto Osellame, Roberta Ramponi, Daniel J. Brod, Ernesto F. Galvão, Nicolò Spagnolo, Chiara Vitelli, Enrico Maiorino, Paolo Mataloni, and Fabio Sciarrino. Integrated multimode interferometers with arbitrary designs for photonic boson sampling. *Nature Photonics*, 7(7):545–549, July 2013.
- [48] Benjamin J. Metcalf, Nicholas Thomas-Peter, Justin B. Spring, Dmytro Kundys, Matthew A. Broome, Peter C. Humphreys, Xian-Min Jin, Marco Barbieri, W. Steven Kolthammer, James C. Gates, Brian J. Smith, Nathan K. Langford, Peter G. R. Smith, and Ian A. Walmsley. Multiphoton quantum interference in a multiport integrated photonic device. *Nature Communications*, 4(1):1356, January 2013. Publisher: Nature Publishing Group.
- [49] Nicolò Spagnolo, Chiara Vitelli, Lorenzo Aparo, Paolo Mataloni, Fabio Sciarrino, Andrea Crespi, Roberta Ramponi, and Roberto Osellame. Three-photon bosonic coalescence in an integrated tritter. *Nature Communications*, 4(1):1606, March 2013. Number: 1 Publisher: Nature Publishing Group.
- [50] Adrian J. Menssen, Alex E. Jones, Benjamin J. Metcalf, Malte C. Tichy, Stefanie Barz, W. Steven Kolthammer, and Ian A. Walmsley. Distinguishability and Many-Particle Interference. *Physical Review Letters*, 118(15):153603, April 2017.
- [51] Benjamin Brecht, Andreas Eckstein, Raimund Ricken, Viktor Quiring, Hubertus Suche, Linda Sansoni, and Christine Silberhorn. Demonstration of coherent time-frequency Schmidt mode selection using dispersion-engineered frequency conversion. *Physical Review A*, 90(3):030302, September 2014. Publisher: American Physical Society.
- [52] B. Brecht, Dileep V. Reddy, C. Silberhorn, and M.G. Raymer. Photon Temporal Modes: A Complete Framework for Quantum Information Science. *Physical Review X*, 5(4):041017, October 2015. Publisher: American Physical Society.
- [53] Laura Serino, Jano Gil-Lopez, Michael Stefszky, Raimund Ricken, Christof Eigner, Benjamin Brecht, and Christine Silberhorn. Realization of a Multi-Output Quantum Pulse Gate for Decoding High-Dimensional Temporal Modes of Single-Photon States. *PRX Quantum*, 4(2):020306, April 2023. Publisher: American Physical Society.
- [54] Patrick Folge, Michael Stefszky, Benjamin Brecht, and Christine Silberhorn. A scheme for fully programmable linear quantum networks based on frequency conversion, February 2024. arXiv:2402.06786 [quant-ph].
- [55] M. E. Marhic, F. S. Yang, L. G. Kazovsky, and Y. Park. Widely tunable spectrum translation and wavelength exchange by four-wave mixing in optical fibers. *Optics Letters*, 21(23):1906, December 1996.
- [56] C. J. McKinstrie, J. D. Harvey, S. Radic, and M. G. Raymer. Translation of quantum states by four-wave mixing in fibers. *Optics Express*, 13(22):9131, 2005.
- [57] H. J. McGuinness, M. G. Raymer, C. J. McKinstrie, and S. Radic. Quantum Frequency Translation of Single-Photon States in a Photonic Crystal Fiber. *Physical Review Letters*, 105(9):093604, August 2010. Publisher: American Physical Society.
- [58] Alex S. Clark, Shayan Shahnia, Matthew J. Collins, Chunle Xiong, and Benjamin J. Eggleton. High-efficiency frequency conversion in the single-photon regime. *Optics Letters*, 38(6):947, March 2013.
- [59] Prathamesh S. Donvalkar, Vivek Venkataraman, Stéphane Clemmen, Kasturi Saha, and Alexander L. Gaeta. Frequency translation via four-wave mixing Bragg scattering in Rb filled photonic bandgap fibers. *Optics Letters*, 39(6):1557, March 2014.
- [60] Imad Agha, Marcelo Davanço, Bryce Thurston, and Kartik Srinivasan. Low-noise chip-based frequency conversion by four-wave-mixing bragg scattering in sinx waveguides. *Opt. Lett.*, 37(14):2997–2999, Jul 2012.
- [61] Qing Li, Marcelo Davanço, and Kartik Srinivasan. Efficient and low-noise single-photon-level frequency conversion interfaces using silicon nanophotonics. *Nature Photonics*, 10(6):406–414, June 2016. Number: 6 Publisher: Nature Publishing Group.
- [62] Bryn A. Bell, Jiakun He, Chunle Xiong, and Benjamin Eggleton. Frequency conversion in silicon in the single photon regime. *Optics Express*, 24(5):5235–5242, 2016.
- [63] Yun Zhao, Bok Young Kim, Xingchen Ji, Yoshitomo Okawachi, Michal Lipson, and Alexander L. Gaeta. High-efficiency on-chip frequency conversion in the telecom band. In *Conference on Lasers and Electro-Optics*, 2022.
- [64] Chaitali Joshi, Alessandro Farsi, Stéphane Clemmen, Sven Ramelow, and Alexander L. Gaeta. Frequency multiplexing for quasi-deterministic heralded single-photon sources. *Nature Communications*, 9(1):847, February 2018.

Supplementary Material

Richard Oliver¹, Miri Blau¹, Chaitali Joshi¹, Xingchen Ji²,
Ricardo Gutiérrez-Jáuregui^{3,4}, Ana Asenjo-Garcia³, Michal Lipson^{1,2}, Alexander L. Gaeta^{1,2}

¹Department of Applied Physics and Applied Mathematics, Columbia University, 500 W
120th St, New York, NY, 10027, US

²Department of Electrical Engineering, Columbia University, 500 W 120th St, New York,
NY, 10027, US

³Department of Physics, Columbia University, 538 W 120th St, New York, NY, 10027, US

⁴Departamento de Física Cuántica y Fotónica, Instituto de Física, Universidad Nacional
Autónoma de México, Ciudad de México, 04510, México

May 16, 2024

1 Classical Derivation of N-Pump BS-FWM

We will consider an electromagnetic wave propagating in a nonlinear fiber. In particular we will model the dynamics of the slowly-varying envelope $A(z, t)$ of the electric field (assuming a single polarization mode)

$$E(\vec{r}, t) = \frac{1}{2} F(x, y) A(z, t) e^{i(\beta_0 z - \omega_0 t)} + c.c., \quad (S1)$$

with spatial mode profile given by $F(x, y)$ and defined with respect to the fast carrier-signal wavevector β_0 and frequency ω_0 . The envelope $A(z, t)$ is well-described classically by the nonlinear Schrödinger equation [1]:

$$\partial_z A(z, t) = \left(i \sum_{m=1}^{\infty} \frac{\beta_m}{m!} (i \partial_t)^m + i \gamma |A(z, t)|^2 \right) A(z, t), \quad (S2)$$

written in terms of the effective nonlinearity γ and the coefficients of the fiber dispersion relation:

$$\beta(\omega) = \sum_m \frac{\beta_m}{m!} (\omega - \omega_0)^m, \quad (S3)$$

where $\beta_m := d^m \beta / d\omega^m|_{\omega_0}$.

The field envelope may be expanded generally into its frequency components:

$$A(z, t) = \sum_j A_j(z) e^{i(\delta\beta_j z - \delta\omega_j t)}, \quad (S4)$$

where $\delta\beta_j := \beta(\omega_j) - \beta_0$ and $\delta\omega_j := \omega_j - \omega_0$ are the wavevector and frequency offsets from those of the carrier. While these frequency components are independent in linear media, they are coupled by optical nonlinearity. This is evident upon inserting Eq. (S4) into Eq. (S2) and matching up Fourier components, which yields:

$$\partial_z A_n(z) = i \gamma \sum_{\substack{k, l, m: \\ \omega_k + \omega_l = \omega_n + \omega_m}} e^{i \Delta\beta_{mn}^{kl} z} A_k(z) A_l(z) A_m^*(z). \quad (S5)$$

In Eq. (S5), we introduce the wavevector mismatch:

$$\Delta\beta_{mn}^{kl} := \beta(\omega_k) + \beta(\omega_l) - \beta(\omega_m) - \beta(\omega_n). \quad (S6)$$

The conditions $\omega_k + \omega_l = \omega_m + \omega_n$ and $\Delta\beta_{mn}^{kl} = 0$ may be interpreted respectively as energy and momentum conservation for a process in which particles k and l collide and reemerge as particles m and n . These conditions constrain the nonlinear interactions contained by the sum in Eq. (S5). Satisfying these constraints is known as phasematching.

The dominant nonlinear processes are those which satisfy momentum conservation, allowing efficient interaction throughout propagation. This may be seen by integrating Eq. (S5) with respect to z to obtain the n^{th} field after a certain propagation distance L :

$$A_n(L) = i\gamma \int_0^L dz \sum_{\substack{k,l,m: \\ \omega_k + \omega_l = \omega_m + \omega_n}} e^{i\Delta\beta_{mn}^{kl}z} A_k(z) A_l(z) A_m^*(z). \quad (S7)$$

Those terms on the RHS for which $\Delta\beta_{mn}^{kl}$ is large in magnitude will carry a rapidly oscillating phasor $e^{i\Delta\beta_{mn}^{kl}z}$; if it oscillates faster than the fields A_j are changing, then the phasor will interfere destructively over the course of the propagation and its contribution to the integral will be negligible. Therefore, only terms for which $\Delta\beta_{mn}^{kl} \ll \sim 1/L$ will be important; all others may be dropped from the sum in the RHS of Eq. (S5). Long propagation lengths typical for fibers are therefore advantageous in constraining the many possible nonlinear processes to those which are desired through phasematching.

So far, we have presented a general description of light propagating in a one-dimensional, dispersive, lossless, third-order nonlinear medium. We now consider our particular setup where the total field consists of high-intensity “pump” fields and low-intensity “weak” fields:

$$A(z, t) = \underbrace{\sum_{p \in P} A_p(z) e^{i(\delta\beta_p z - \delta\omega_p t)}}_{\text{pumps}} + \underbrace{\sum_{s \in S} b_s(z) e^{i(\delta\beta_s z - \delta\omega_s t)}}_{\text{weak fields}}. \quad (S8)$$

Here, P and S denote the set of pump and weak fields, respectively. (The weak fields will later become the signal and idler fields in two-pump Bragg scattering.) First, let us recall the case of Bragg scattering with two pumps [2, 3, 4]; in order for this process to be phasematched it is sufficient to situate the pumps and the weak signal/idler fields approximately symmetrically about the zero-group velocity dispersion frequency ω_{ZGVD} , defined by $\beta_2(\omega_{ZGVD}) := 0$. Since the nonlinear medium couples different weak fields in pairs, the case of N pumps considered in this work requires that each pair of pumps be displaced symmetrically from the corresponding pair of weak fields about ω_{ZGVD} [4].

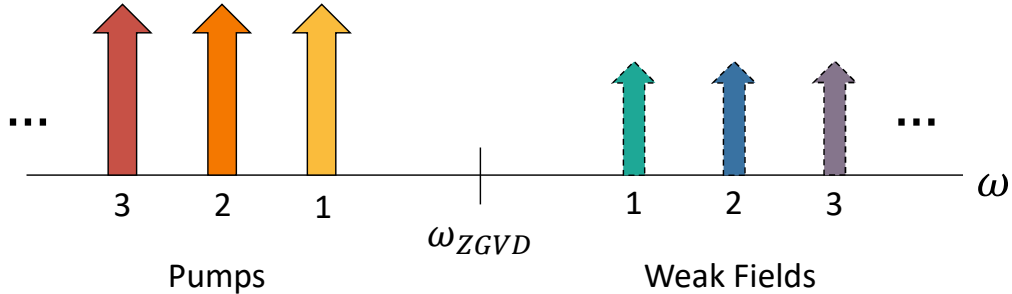


Figure 1: Phasematching requires symmetric locations of the pumps and weak signal/idler frequencies about the zero-group velocity dispersion frequency, ω_{ZGVD} .

Motivated by this phasematching scheme, we consider an array of N pumps mixing N weak fields, shown in Fig. 1 along with the labeling convention. We start by finding the steady-state solution for the pump fields. Starting from Eq. (S5) we include only phasematched terms under the approximation that contributions due to the weak fields are negligible compared to those of the pumps themselves and cannot appreciably remove energy from the pump modes. This results in:

$$\partial_z A_n(z) = i\gamma \left(\overbrace{|A_n(z)|^2}^{\text{self-phase}} + \sum_{p \neq n} \overbrace{2|A_p(z)|^2}^{\text{cross-phase}} \right) A_n(z). \quad (S9)$$

From Eq. (S9) it follows that

$$\partial_z |A_n(z)|^2 = A_n^*(z) \partial_z A_n(z) + c.c. = 0; \quad (\text{S10})$$

this yields $|A_n(z)| = |A_n(0)|$. The pump fields therefore only change by a phase. This is a consequence of the above approximation in which weak field contributions to pumps dynamics were neglected. Because this implies that the pump fields cannot lose energy it is known as the undepleted-pump approximation [5]. This approximation is particularly reliable for BS-FWM since only a relatively small and finite amount of power is taken from the pumps in the conversion from signal to idler. This power is a fraction at most $\sim \frac{P_{sig}(\omega_{idl}-\omega_{sig})}{P_{pump}\omega_{sig}} \ll 1$.

Proceeding, the solution to Eq. (S9) is given in terms of the initial pump amplitudes:

$$A_n(z) = e^{i\Gamma_n z} A_n(0), \quad (\text{S11})$$

$$\Gamma_n = \gamma(|A_n(0)|^2 + 2 \sum_{p \neq n} |A_p(0)|^2). \quad (\text{S12})$$

Turning now to the weak-field dynamics, Eq. (S5) leads to:

$$\partial_z b_n(z) = i\gamma \left(\sum_p \overbrace{2|A_p(z)|^2 b_n(z)}^{\text{cross-phase}} + \sum_{\left\{ \begin{smallmatrix} j,k,l: \\ l \neq n, \\ \omega_j + \omega_l = \\ \omega_k + \omega_n \end{smallmatrix} \right\}} \overbrace{2e^{i\Delta\beta_{kn}^{jl} z} A_j(z) A_k^*(z) b_l(z)}^{\text{Bragg-scattering}} \right), \quad (\text{S13})$$

where, as with the pumps, terms higher than lowest order in the weak fields may be neglected (due to the large intensity of the pump fields). Using Ω_i and ω_i for the i^{th} pump and weak-field frequency respectively, the above may be simplified considerably on rewriting the energy conservation condition: $\Omega_j + \omega_l = \Omega_k + \omega_n$. From the assumed configuration of frequencies, energy and momentum are both conserved only when $j = l$ and $k = n$. Thus we may write:

$$\sum_{\left\{ \begin{smallmatrix} j,k,l: \\ l \neq n, \\ \omega_j + \omega_l = \\ \omega_k + \omega_n \end{smallmatrix} \right\}} \rightarrow \sum_{\left\{ \begin{smallmatrix} j,k,l: \\ l \neq n \end{smallmatrix} \right\}} \delta_{jl} \delta_{kn}. \quad (\text{S14})$$

Then defining the N rotating frames

$$\bar{b}_n(z) := b_n(z) e^{i\varphi_n z}, \quad (\text{S15})$$

$$\varphi_n := \Delta\beta_1^n + \gamma(P_1 - P_n - 2 \sum_p P_p), \quad (\text{S16})$$

$$\Delta\beta_m^n := \beta(\Omega_n) + \beta(\omega_n) - \beta(\Omega_m) - \beta(\omega_m), \quad (\text{S17})$$

where $P_p = |A_p(0)|^2$ is the power of the p^{th} pump, one obtains the simpler form

$$\partial_z \bar{b}_n(z) = i\Delta k_n \bar{b}_n(z) + 2i\gamma \sum_{l \neq n} A_l(0) A_n^*(0) \bar{b}_l(z), \quad (\text{S18})$$

where Δk_n is the nonlinear phase mismatch:

$$\Delta k_n := \Delta\beta_1^n + \gamma(P_1 - P_n). \quad (\text{S19})$$

It is then evident that the weak fields undergo unitary evolution via the matrix equation

$$\partial_z \begin{bmatrix} \bar{b}_1(z) \\ \vdots \\ \bar{b}_N(z) \end{bmatrix} = i \begin{bmatrix} 0 & & & 2\gamma A_i^*(0) A_j(0) \\ & \Delta k_2 & & \\ & & \ddots & \\ 2\gamma A_i^*(0) A_j(0) & & & \Delta k_N \end{bmatrix} \begin{bmatrix} \bar{b}_1(z) \\ \vdots \\ \bar{b}_N(z) \end{bmatrix}, \quad (\text{S20})$$

which reduces to the conventional Bragg-scattering transformation [2] for $N = 2$ as expected. Note that the dependence on relative pump phases in Eq. (S20) can be factored out of the transformation by rewriting Eq. (S18):

$$\partial_z \bar{b}_n(z) = i \sum_l \left[\delta_{nl} (\Delta k_n - 2\gamma P_n) + 2\gamma \sqrt{P_n P_l} \right] e^{i(\theta_l - \theta_n)} \bar{b}_l(z), \quad (\text{S21})$$

with the relative phases θ_i , defined by $A_n(0) = \sqrt{P_n} e^{i\theta_n}$, inherited from the pump fields.

For simplicity, we consider the case of perfect phasematching $\Delta k_n = 0$ and uniform pump powers, $P_n = P$. The propagation equation is then (factoring out the relative pump phases θ_n and grouping them with the \bar{b}_n):

$$\partial_z \begin{bmatrix} \bar{b}_1(z) e^{i\theta_1} \\ \vdots \\ \bar{b}_N(z) e^{i\theta_N} \end{bmatrix} = 2i\gamma P \begin{bmatrix} 0 & 1 & 1 \\ 1 & \ddots & 1 \\ 1 & 1 & 0 \end{bmatrix} \begin{bmatrix} \bar{b}_1(z) e^{i\theta_1} \\ \vdots \\ \bar{b}_N(z) e^{i\theta_N} \end{bmatrix}. \quad (\text{S22})$$

The solution¹ at $z = L$ is given in terms of the nonlinear phase $\phi = 2\gamma LP$:

$$\begin{bmatrix} \bar{b}_1(L) e^{i\theta_1} \\ \vdots \\ \bar{b}_N(L) e^{i\theta_N} \end{bmatrix} = e^{-i\phi} \begin{bmatrix} p_N(\phi) & & q_N(\phi) \\ & \ddots & \\ q_N(\phi) & & p_N(\phi) \end{bmatrix} \begin{bmatrix} \bar{b}_1(0) e^{i\theta_1} \\ \vdots \\ \bar{b}_N(0) e^{i\theta_N} \end{bmatrix}, \quad (\text{S23})$$

where

$$q_N(\phi) = \frac{e^{iN\phi} - 1}{N}, \quad (\text{S24})$$

$$p_N(\phi) = q_N(\phi) + 1. \quad (\text{S25})$$

Observe that the combined power from all N pumps contributes to the total nonlinear phase; it is $N\phi$ that dictates the conversion strength.

1.1 Incorporating Loss

To understand the effects of propagation loss for the case of perfect phasematching with N pumps of equal initial power, we modify the dynamics of the pumps and weak fields as follows:

$$\partial_z A_n(z) = \left(-\alpha + i\gamma (|A_n(z)|^2 + \sum_{p \neq n} 2|A_p(z)|^2) \right) A_n(z), \quad (\text{S26})$$

$$\partial_z b_n(z) = \left(-\alpha + 2i\gamma \sum_p |A_p(z)|^2 \right) b_n(z) + 2i\gamma \sum_{l \neq n} A_l(z) A_n^*(z) b_l(z). \quad (\text{S27})$$

Using the same technique as Eq. (S10), it follows that $|A_n(z)| = e^{-\alpha z} |A_n(0)|$, and reinserting this with $A_n(0) = \sqrt{P} e^{i\theta_n}$ one obtains a loss-dependent nonlinear phase for the pumps:

$$A_n(z) = \sqrt{P} e^{i\theta_n} e^{-\alpha z + i\phi_\alpha(z)(N-1/2)}, \quad (\text{S28})$$

where:

$$\phi_\alpha(z) = 2\gamma P z e^{-\alpha z} \text{sinhc}(\alpha z). \quad (\text{S29})$$

The dynamics of the weak fields then become:

$$\partial_z b_n(z) = \left(-\alpha + 2i\gamma N P e^{-2\alpha z} \right) b_n(z) + 2i\gamma P e^{-2\alpha z} \sum_{l \neq n} e^{i\theta_l - i\theta_n} b_l(z). \quad (\text{S30})$$

¹Note that for the N -dimensional matrix defined by $O_{ij} = 1$, it follows that $O^2 = NO$.

In the frame $\tilde{b}_n(z) := e^{\alpha z + i\theta_n} b_n(z)$, this simplifies to:

$$\partial_z \tilde{b}_n(z) = 2i\gamma N P e^{-2\alpha z} \tilde{b}_n(z) + 2i\gamma P e^{-2\alpha z} \sum_{l \neq n} \tilde{b}_l(z). \quad (\text{S31})$$

This is a matrix equation of the form $\partial_z \vec{\tilde{b}}(z) = iH(z) \vec{\tilde{b}}(z)$. Since $[H(z), H(z')] = 0$, we may directly integrate:

$$\vec{\tilde{b}}(z) = e^{i \int_0^z dz' H(z')} \vec{\tilde{b}}(0). \quad (\text{S32})$$

Repeating the above procedures, the solution is:

$$b_n(z) = \sum_l e^{-\alpha z + i[-\theta_n + \theta_l + i\phi_\alpha(z)(N-1)]} \left(\frac{e^{i\phi_\alpha(z)} - 1}{N} + \delta_{nl} \right) b_l(0). \quad (\text{S33})$$

Note that, for a single-mode input in mode k , the intensity is given by:

$$|b_n(z)|^2 = e^{-2\alpha z} \left| \frac{e^{i\phi_\alpha(z)} - 1}{N} + \delta_{nk} \right|^2. \quad (\text{S34})$$

In this experiment, the propagation length is fixed at $z = L$; only the initial pump power P is varied. The resulting singles counts (measuring relative intensities versus pump power) for each channel are therefore scaled by one, *constant* factor of $e^{2\alpha z}$ with a scaled nonlinear phase ($\phi_\alpha(z)$ instead of $\phi(z)$). That is, the intensity curves are identical to the lossless solutions up to a vertical and horizontal scale. In this experiment, propagation losses are quoted from the Vistacor datasheet provided by Corning: having at most 0.43 dB/km at 1285 nm, the 100-m fiber has a total loss of $e^{-2\alpha L} \approx 1\%$. This justifies the use of the lossless theory curves to fit the intensities (described later in further detail), with the understanding that any corrections under the above assumptions merely augment the vertical and horizontal scales minimally (about 1% and 0.5%, respectively).

1.2 Case of $N = 3$

In our experiment we study the case of Bragg scattering with three pumps. We set the pump powers to be equal and choose frequencies such that $\Delta k_2 = 0$ and Δk_1 is negligible compared to π/L , where L is the interaction length (100 m in this experiment). Setting $N = 3$ we have the solution:

$$\begin{bmatrix} b_1(L)e^{i\theta_1} \\ b_2(L)e^{i\theta_2} \\ b_3(L)e^{i\theta_3} \end{bmatrix} = e^{2i\phi} \begin{bmatrix} p(\phi) & q(\phi) & q(\phi) \\ q(\phi) & p(\phi) & q(\phi) \\ q(\phi) & q(\phi) & p(\phi) \end{bmatrix} \begin{bmatrix} b_1(0)e^{i\theta_1} \\ b_2(0)e^{i\theta_2} \\ b_3(0)e^{i\theta_3} \end{bmatrix}, \quad (\text{S35})$$

where, as above, $\phi = 2\gamma LP$ is the nonlinear phase and

$$q(\phi) = \frac{e^{3i\phi} - 1}{3} \quad (\text{S36})$$

$$p(\phi) = q(\phi) + 1. \quad (\text{S37})$$

1.3 Bragg-Scattering for Quantized Fields

The quantized displacement field may be written (for instance, see [6]):

$$\hat{D}(\vec{r}, t) = \int d\beta \sqrt{\frac{\hbar\omega(\beta)}{4\pi}} \hat{a}(\beta, t) d(x, y) e^{i\beta z} + h.c., \quad (\text{S38})$$

where the field is approximated as exciting only the fundamental linearly polarized mode (e.g. HE_{01}) of the nonlinear fiber, with longitudinal coordinate z . In the above definition $\hat{a}(\beta, t)$ annihilates a plane wave with propagation constant β at time t , having the equal-time commutator:

$$[\hat{a}(\beta, t), \hat{a}^\dagger(\beta', t)] = \delta(\beta - \beta'). \quad (\text{S39})$$

Using the definition of the slowly-varying envelope in terms of which the NLSE is written [1],

$$E(\vec{r}, t) = \frac{1}{2} F(x, y) A(z, t) e^{i(\beta_0 z - \omega_0 t)} + c.c., \quad (\text{S40})$$

and the respective spatial mode normalizations of [6] and [1],

$$\int dx dy \frac{|d(x, y)|^2}{\epsilon_0 \epsilon(\omega)} \frac{v_p(\omega)}{v_g(\omega)} = 1 = \int dx dy \frac{|F(x, y)|^2}{\mathcal{A}}, \quad (\text{S41})$$

(where v_p , v_g are phase and group velocities and \mathcal{A} is the effective mode area), we identify the quantized slowly-varying envelope operator:

$$\hat{A}(z, t) = \int d\beta \sqrt{\frac{\hbar \omega(\beta) v_g}{\pi \mathcal{A} \epsilon_0 \epsilon(\beta) v_p}} \hat{a}(\beta, t) e^{i(\beta - \beta_0)z + i\omega_0 t}. \quad (\text{S42})$$

With the definition Eq. (S8) we may decompose the slowly-varying envelope into bands corresponding to the longitudinal envelope annihilation operator of the i^{th} weak field:

$$\hat{b}_i(z, t) = \int_{\beta_i - \Delta\beta/2}^{\beta_i + \Delta\beta/2} d\beta \sqrt{\frac{\hbar \omega(\beta) v_g}{\pi \mathcal{A} \epsilon_0 \epsilon(\beta) v_p}} \hat{a}(\beta, t) e^{i(\beta - \beta_i)z + i\omega_i t}, \quad (\text{S43})$$

in correspondence with the classical fields b_i in which the Bragg-scattering transformation Eq. (S13) is written (note the relative factor of $e^{i\delta\beta_i z - i\delta\omega_i t}$ between Eqs. (S43) and (S42)). Neglecting the frequency dependence of the root in the integrand of Eq. (S43), we rewrite the longitudinal envelope operator as

$$\hat{b}_i(z, t) \approx \sqrt{C} \int_{-\Delta\beta/2}^{\Delta\beta/2} \frac{d\beta}{\sqrt{2\pi}} \hat{a}_i(\beta, 0) e^{i\beta z - i(\omega(\beta_i + \beta) - \omega_i)t}, \quad (\text{S44})$$

where

$$\hat{a}_i(\beta, t) := \hat{a}(\beta_i + \beta, t), \quad (\text{S45})$$

$$\text{and } C := \frac{2\hbar\omega_0 v_{g,0}}{\mathcal{A}\epsilon_0\epsilon(\omega_0)v_{p,0}}. \quad (\text{S46})$$

The free (i.e. non-interacting) spatial annihilation operators may then be defined as:

$$\hat{a}_i(z, t) := \int_{-\Delta\beta/2}^{\Delta\beta/2} \frac{d\beta}{\sqrt{2\pi}} \hat{a}_i(\beta, 0) e^{i\beta z - i(\omega(\beta_i + \beta) - \omega_i)t} \quad (\text{S47})$$

$$[\hat{a}_i(z, t), \hat{a}_j^\dagger(z', t')] \approx \delta_{ij} \delta(z - z' - v_{g,i}(t - t')). \quad (\text{S48})$$

Because the classical equation of motion Eq. (S20) is linear in the weak fields, the classical and quantum dynamics are identical. We may therefore replace the classical interacting fields with bosonic annihilation operators in the Heisenberg picture. *In the interaction region* (i.e. the nonlinear medium), under the assumptions of negligible phase mismatch and equal pump powers, the position operators at propagation distance $z = L$ and $z = 0$ are related by²:

$$\hat{a}_i(L, t) = \sum_j U_{ij}(\phi) \hat{a}_j(0, t - L/v_g), \quad (\text{S49})$$

where $U_{ij}(\phi)$ is given from Eq. (S35) as

$$U_{ij}(\phi) = \begin{cases} p(\phi) & i = j \\ q(\phi) e^{i(\theta_j - \theta_i)} & i \neq j. \end{cases} \quad (\text{S50})$$

The phase factor $e^{2i\phi}$ from Eq. (S35) is a global phase at a given propagation length L and may be absorbed into the definition of $\hat{a}_i(L, t)$.

²(Taking the group velocities as approximately constant, $v_{g,i} \approx v_g$.)

2 Correlation Functions

The spectrally filtered field measured at one of the detectors corresponds to the operator $\hat{a}_i(z, t)$, where $i \in \{1, 2, 3\}$ denotes one of the three interacting frequency modes. The singles rates are then proportional to the first-order correlation function at the detectors given by the expectation:

$$G_i^{(1)}(z) = \langle \psi | \hat{a}_i^\dagger(z, t) \hat{a}_i(z, t) | \psi \rangle. \quad (\text{S51})$$

Coincidence rates are proportional to the second-order correlation function:

$$G_{ij}^{(2)}(z, \tau) = \langle \psi | \hat{a}_j^\dagger(z, t) \hat{a}_i^\dagger(z, t + \tau) \hat{a}_i(z, t + \tau) \hat{a}_j(z, t) | \psi \rangle. \quad (\text{S52})$$

To compute the total coincidence count rate we integrate the coincidence histogram over the inverse linewidth of the photon pair source (with respect to the event delay time, τ). Since the integration washes out the temporal dependence of the fields and absorbs the Dirac-delta functions in the field commutators, for simplicity we adopt a discrete-mode model by using the following replacement rules:

$$\begin{aligned} \hat{a}_i(z, t) &\rightarrow \hat{a}_i(z) \\ [\hat{a}_i(z, t), \hat{a}_j^\dagger(z, t')] &= \delta_{ij} \delta(t - t') / v_{g,i} \rightarrow [\hat{a}_i(z), \hat{a}_j^\dagger(z)] = \delta_{ij} \end{aligned}$$

Thus, the integrated first and second-order correlation functions may be computed using:

$$G_i^{(1)}(z) = \langle \psi | \hat{a}_i^\dagger(z) \hat{a}_i(z) | \psi \rangle = ||\hat{a}_i(z) | \psi \rangle||^2, \quad (\text{S53})$$

$$G_{ij}^{(2)}(z) = \langle \psi | \hat{a}_j^\dagger(z) \hat{a}_i^\dagger(z) \hat{a}_i(z) \hat{a}_j(z) | \psi \rangle = ||\hat{a}_i(z) \hat{a}_j(z) | \psi \rangle||^2. \quad (\text{S54})$$

The discrete-mode model contains the essential physics necessary to compute the coincidence rates as a function of nonlinear phase. In order to investigate finer temporal dependence (e.g. to compute the dependence of the correlation function on delay time τ), the time dependence would need to be retained.

2.1 Classical Input

2.1.1 Single-Mode Coherent State

For the coherent state $|\nu_1\rangle = e^{\nu_1 \hat{a}_1^\dagger(z=0) - h.c.} |0\rangle$ occupying the first frequency mode as input, the singles rates at $z = L$ are given by:

$$G_i^{(1)}(z) = \langle \nu_1 | \hat{a}_i^\dagger(L) \hat{a}_i(L) | \nu_1 \rangle. \quad (\text{S55})$$

Using the linear transformation $\hat{a}_i(z) = \sum_k U_{ik}(z) \hat{a}_k(0)$ where $\hat{a}_i(0)$ denotes the i^{th} field before interaction, we may write

$$G_i^{(1)}(z) = ||\sum_j U_{ij}(z) \hat{a}_j(0) | \nu_1 \rangle||^2 = |U_{i1}(z)|^2 |\nu_1|^2. \quad (\text{S56})$$

Explicitly, in terms of the nonlinear phase $\phi = 2\gamma LP$:

$$\begin{aligned} G_1^{(1)}(\phi) &= |\nu_1|^2 |U_{11}(\phi)|^2 = |\nu_1|^2 |p(\phi)|^2, \\ G_2^{(1)}(\phi) &= G_3^{(1)}(\phi) = |\nu_1|^2 |U_{21}(\phi)|^2 = |\nu_1|^2 |q(\phi)|^2. \end{aligned} \quad (\text{S57})$$

2.1.2 Dual-Mode Coherent State

For a dual-mode CW coherent state (omitting the z argument, $\hat{a} := \hat{a}(z = 0)$)

$$|\nu_1, 0, \nu_3\rangle = e^{\nu_1 \hat{a}_1^\dagger + \nu_3 \hat{a}_3^\dagger - h.c.} |0\rangle, \quad (\text{S58})$$

the first-order correlation function following the interaction is

$$\begin{aligned} G_i^{(1)}(z) &= \left\| \sum_j U_{ij}(z) \hat{a}_j \right\| \nu_1, 0, \nu_3 \right\|^2 \\ &= |U_{i1}(z)\nu_1 + U_{i3}(z)\nu_3|^2. \end{aligned} \quad (\text{S59})$$

Since in our experiment the relative phase between the two coherent states is not fixed, we write $\nu_3 = \nu_1 e^{i\vartheta(t-\beta_1 z)}$. Final results must then be averaged over the independent classical random variables $\vartheta(t-\beta_1 z)$ (i.e. the relative phases $\{\vartheta_k\}$ during the k^{th} interaction window), uniformly distributed over $[0, 2\pi)$. Since the pump phases θ_i contained in U_{ij} are also randomly fluctuating, these too must be averaged over. Finally, in our experiment we choose $|\nu_1| = |\nu_3| = \nu$. Using the above formalism, after averaging we obtain:

$$\begin{aligned} G_1^{(1)}(z) &= G_3^{(1)}(z) = \nu^2 (|p(z)|^2 + |q(z)|^2) \\ &= \nu^2 (1 - |q(z)|^2) \\ G_2^{(1)}(z) &= 2\nu^2 |q(z)|^2. \end{aligned} \quad (\text{S60})$$

The total coincidence rate is³:

$$\begin{aligned} G_{ij}^{(2)}(z) &= \left\| \hat{a}_i(z) \hat{a}_j(z) \right\| \nu_1, 0, \nu_3 \right\|^2 \\ &= |(U_{i1}(z)\nu_1 + U_{i3}(z)\nu_3)(U_{j1}(z)\nu_1 + U_{j3}(z)\nu_3)|^2 \\ &= G_i^{(1)}(z) G_j^{(1)}(z). \end{aligned} \quad (\text{S61})$$

We define a normalized coincidence rate as:

$$g_{ij}^{(2)}(\phi) := \frac{G_{ij}^{(2)}(\phi)}{G_{ij}^{(2)}(0)}. \quad (\text{S62})$$

The normalized coincidence for ports one and three is then:

$$g_{13}^{(2)}(\phi) = (1 - |q(\phi)|^2)^2. \quad (\text{S63})$$

2.2 Photon-Pair Input

Consider now the two-photon state as input:

$$|\psi(0)\rangle = \hat{a}_1^\dagger(0) \hat{a}_3^\dagger(0) |0\rangle. \quad (\text{S64})$$

The singles rates are given by:

$$G_i^{(1)}(z) = |U_{i1}(z)|^2 + |U_{i3}(z)|^2. \quad (\text{S65})$$

Note that this expression is identical to that of two coherent states that are mutually phase-incoherent.

The coincidence rates, however, are given by:

$$G_{ij}^{(2)}(\phi) = |U_{i1}(\phi)U_{j3}(\phi) + U_{i3}(\phi)U_{j1}(\phi)|^2. \quad (\text{S66})$$

The coherent sum appearing in this expression reflects the indistinguishability of the two photons; the two terms account for the amplitudes that the photons exiting at the i^{th} and j^{th} ports originated respectively from input ports 1 and 3 or vice versa.

The normalized coincidence rate is then:

$$g_{13}^{(2)}(\phi) = |p^2(\phi) + q^2(\phi)|^2, \quad (\text{S67})$$

$$g_{12}^{(2)}(\phi) = g_{23}^{(2)}(\phi) = |p(\phi)q(\phi) + q^2(\phi)|^2. \quad (\text{S68})$$

³Note that, before integrating out the explicit time dependence, the coinciding events at detectors i and j occur at some delay τ ; therefore the relative phase variables $\{\vartheta(t), \vartheta(t+\tau)\}$ are independent when averaged over all interaction windows.

2.3 Including Multiphoton Effects and Loss

Using the simplified discrete-mode model it is straightforward to incorporate the multiphoton contribution inherent in photon-pair generation as well as system insertion losses.

The spontaneous four-wave mixing process used in our experiment to generate photon pairs can be modeled using a two-mode squeezed vacuum state $|\zeta\rangle = \hat{U}(\zeta)|0\rangle$ where

$$\hat{U}(\zeta) = e^{\zeta \hat{a}_1^\dagger(0) \hat{a}_3^\dagger(0) - h.c.} \quad (\text{S69})$$

Evolving the fields as $\hat{a}_i(\zeta) := \hat{U}^\dagger(\zeta) \hat{a}_i(0) \hat{U}(\zeta)$, the squeezing operator \hat{U} leads to the following transformation in the Heisenberg picture:

$$\begin{bmatrix} \hat{a}_1(\zeta) \\ \hat{a}_3^\dagger(\zeta) \end{bmatrix} = \begin{bmatrix} \cosh(|\zeta|) & \frac{\zeta}{|\zeta|} \sinh(|\zeta|) \\ \frac{\zeta^*}{|\zeta|} \sinh(|\zeta|) & \cosh(|\zeta|) \end{bmatrix} \begin{bmatrix} \hat{a}_1(0) \\ \hat{a}_3^\dagger(0) \end{bmatrix}. \quad (\text{S70})$$

We include loss using a beamsplitter model which couples a given fiber mode \hat{a}_i to its own external vacuum mode with annihilator \hat{r}_i :

$$\hat{U}(\alpha) = e^{\Sigma_i \alpha_i \hat{a}_i^\dagger \hat{r}_i - h.c.} \quad (\text{S71})$$

The loss may be regarded as equivalent to a non-unit transmission coefficient, $T_i = \cos(|\alpha_i|)$, corresponding to a reflection coefficient $R_i = \frac{\alpha_i}{|\alpha_i|} \sin(|\alpha_i|)$. The Heisenberg-picture transformation is then given by:

$$\begin{bmatrix} \hat{a}_i(\alpha) \\ \hat{r}_i(\alpha) \end{bmatrix} = \begin{bmatrix} T_i & R_i \\ -R_i^* & T_i \end{bmatrix} \begin{bmatrix} \hat{a}_i(0) \\ \hat{r}_i(0) \end{bmatrix}. \quad (\text{S72})$$

We account for losses before and after the Bragg-scattering interaction using the parameters α_i and μ_i respectively.

The full evolution of the state prior to detection is then given by

$$|\psi\rangle_{\text{final}} = \hat{U}(\mu) \hat{U}(\phi) \hat{U}(\alpha) \hat{U}(\zeta) |0\rangle, \quad (\text{S73})$$

where ζ and ϕ parametrize the squeezing and Bragg-scattering evolution, respectively.

The singles rates are given by

$$\begin{aligned} G_i^{(1)}(\phi) &= \|\hat{a}_i \hat{U}(\mu) \hat{U}(\phi) \hat{U}(\alpha) \hat{U}(\zeta) |0\rangle\|^2 \\ &= |T_i(\mu)|^2 \sinh^2(|\zeta|) \sum_{j \neq 2} |U_{ij}(\phi) T_j(\alpha)|^2. \end{aligned} \quad (\text{S74})$$

The coincidences are given by

$$\begin{aligned} G_{ij}^{(2)} &= \|\hat{a}_i \hat{a}_j \hat{U}(\mu) \hat{U}(\phi) \hat{U}(\alpha) \hat{U}(\zeta) |0\rangle\|^2 \\ &= |T_i(\mu)|^2 |T_j(\mu)|^2 |T_1(\alpha)|^2 |T_3(\alpha)|^2 \\ &\quad \times \left\{ \left| U_{i,1}(\phi) U_{j,3}(\phi) + U_{i,3}(\phi) U_{j,1}(\phi) \right|^2 \left(\sinh^2(|\zeta|) + 2 \sinh^4(|\zeta|) \right) \right. \\ &\quad \left. + 2 \left(|U_{i,1}(\phi)|^2 |U_{j,1}(\phi)|^2 \frac{|T_1(\alpha)|^2}{|T_3(\alpha)|^2} + |U_{i,3}(\phi)|^2 |U_{j,3}(\phi)|^2 \frac{|T_3(\alpha)|^2}{|T_1(\alpha)|^2} \right) \sinh^4(|\zeta|) \right\}. \end{aligned} \quad (\text{S75})$$

Inserting the expressions for $U_{ij}(\phi)$ from Eq. (S50), we obtain the normalized coincidence rate (considering for simplicity only coincidences between output frequency modes one and three):

$$\begin{aligned} g_{13}^{(2)}(\phi) &= |p^2(\phi) + q^2(\phi)|^2 \\ &\quad + 2|p(\phi)|^2 |q(\phi)|^2 \left(\frac{|T_1(\alpha)|^2}{|T_3(\alpha)|^2} + \left| \frac{T_3(\alpha)}{T_1(\alpha)} \right|^2 \right) \left(\frac{\sinh^2(|\zeta|)}{1 + 2 \sinh^2(|\zeta|)} \right). \end{aligned} \quad (\text{S76})$$

By taking the photon-pair limit of this expression, one obtains the two-photon prediction of Eq. (S67). The first term in the RHS therefore corresponds to photon-pair statistics, and the second may be understood as originating from multiphoton effects. Note that appearance of asymmetry in the input losses $T_i(\alpha)$ only enters via the multiphoton term. This is physically intuitive since, in the photon-pair limit, when one photon in the pair is lost the coincidence is not counted; so normalized coincidence rates do not depend on loss asymmetry. With multiphoton effects, however, even when one photon is lost coincidences may still be registered.

The resulting theoretical normalized coincidences of the classical two-mode input (phase-averaged coherent states) and photon-pair input (including multiphoton contribution with symmetric losses) are plotted in Fig. 2. Whereas the classical curves are given by the products of the two uncorrelated singles rates, for photon pairs an interference effect is predicted. This contrast in coincidence rates comes about due to the interference of amplitudes corresponding to interchangeable two-photon states, and may be interpreted as a Hong-Ou-Mandel effect.

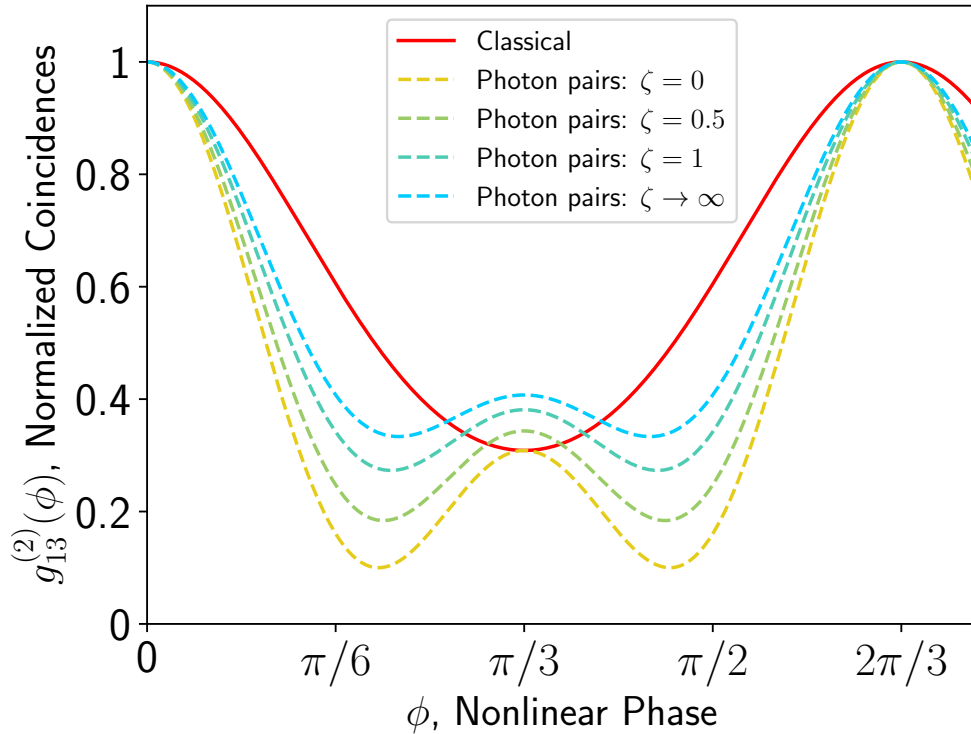


Figure 2: Theoretical coincidence rates for two classical (coherent-state) inputs and a photon-pair input interfering via the three-way Bragg scattering interaction. ζ represents the multiphoton parameter.

3 Measurement of Model Parameters

3.1 Losses Before Nonlinear Fiber

According to Eq. (S76), to account for the contributions due to multiphoton statistics it is necessary to incorporate the ratio of losses accumulated between generation and before Bragg scattering. We estimate these losses using measurements concurrent with the experiment. The dominant sources of loss originate from wavelength-dependent asymmetries in the filtering setup prior to the nonlinear fiber. To measure the ratio of the losses before the fiber, we first measure the relative insertion losses of the filtering setup following the nonlinear fiber. We then factor this out of the singles rates measured during each trial. Assuming negligible

differences in SNSPD detection efficiency, this results in an estimate of the loss ratio prior to entering the fiber. We can then use this measurement in our model Eq. (S76), eliminating an otherwise free parameter.

3.2 Multiphoton Parameter

We generate photon pairs using spontaneous four-wave mixing by pumping a single resonance (at approximately 1282.8 nm) of an integrated SiN microresonator. Microscopically, two pump photons are annihilated and correlated photons with frequencies at $\pm\Delta\omega$ are created. However, photon pairs are only the leading-order effect; the full state contains multiphoton terms and is better described by the two-mode squeezed vacuum (see e.g. [7]):

$$|\zeta\rangle = e^{\zeta\hat{a}_+^\dagger\hat{a}_-^\dagger - h.c.} |0\rangle = \text{sech}(|\zeta|) \sum_{n=0}^{\infty} \left(\frac{\zeta}{|\zeta|} \tanh(|\zeta|) \right)^n |n, n\rangle. \quad (\text{S77})$$

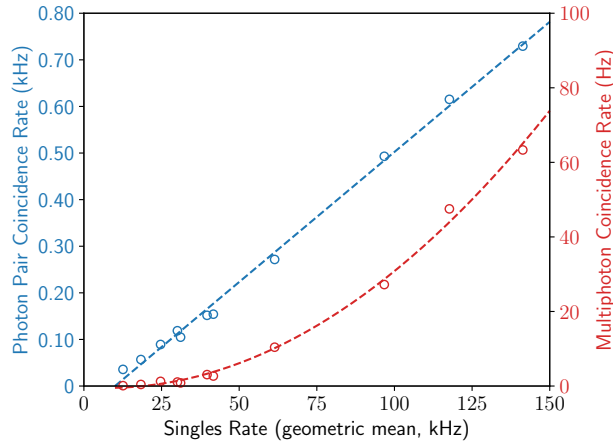


Figure 3: Scaling of photon-pair and multiphoton coincidences with singles rate. Dashed lines indicate linear and quadratic fits to the data (circles).

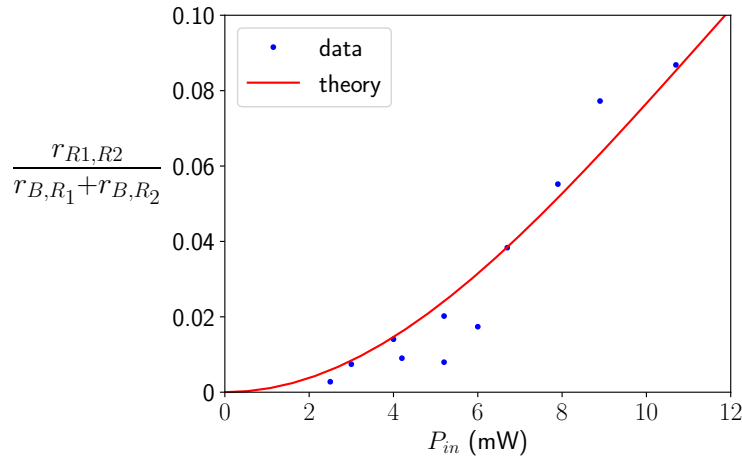


Figure 4: Ratio of multiphoton coincidences (B1-B2) to dual-frequency coincidences (A-B1 plus A-B2).

To estimate $|\zeta|$, we measure multiphoton coincidences as a function of pump power. The output of the ring is first spectrally filtered into two channels, R (red photon, 1285.0 nm) and B (blue photon, 1280.6

nm). (The freespace filtering setup after the nonlinear fiber is used rather than fiber-Bragg gratings; this helps avoid introducing the loss asymmetry described above.) Channel R is then sent through a 50:50 fiber beamsplitter resulting in two output channels, R1 and R2. If only pairs of single photons (i.e., $|1, 1\rangle$) were present, then no coincidences should be registered between channels R1 and R2; only B-R1 and B-R2 coincidences would be detected. R1-R2 coincidences therefore serve to characterize the multiphoton emission. In Fig. 3 are plotted multiphoton ($r_{R1,R2}$) and photon pair ($r_{B,R1} + r_{B,R2}$) coincidence rates versus singles rates ($\sqrt{r_B(r_{R1} + r_{R2})}$). The expected scaling is observed: photon-pair coincidences scale linearly with the singles rate, $r_{pair} \propto r_{sgls} \propto |\zeta|^2$, whereas multiphoton coincidences are approximately quadratic, $r_{mult} \propto r_{sgls}^2 \propto |\zeta|^4$. Corresponding linear and quadratic fits are plotted in agreement with theory.

SFWM pump power is varied from 2.5 to 10.7 mW (measured before the chip). The experiment is performed at 10.8 mW of pump power. Multiphoton emission is characterized by plotting the ratio of R1-R2 coincidences to the sum of B-R1 and B-R2 coincidences. The results are shown in Fig. 4. From fitting to the analytical curve we obtain $|\zeta| \approx 0.4$.

4 Data Analysis

4.1 Single-Frequency Input

In order to compare experiment with theory, we perform least-squares fits of detection events as a function of peak pump power to the sinusoidal curves obtained analytically under the assumptions of equal pump powers, zero phase mismatch ($\Delta k_n = 0$), and lossless nonlinear fiber.

The raw singles rates obtained for classical single-frequency input in Fig. 5 are for each data point normalized to the input signal rate at zero pump power (i.e. without Bragg scattering). It is necessary to convert from measured peak powers of the Bragg pumps to nonlinear phase in order to fix the horizontal scale.

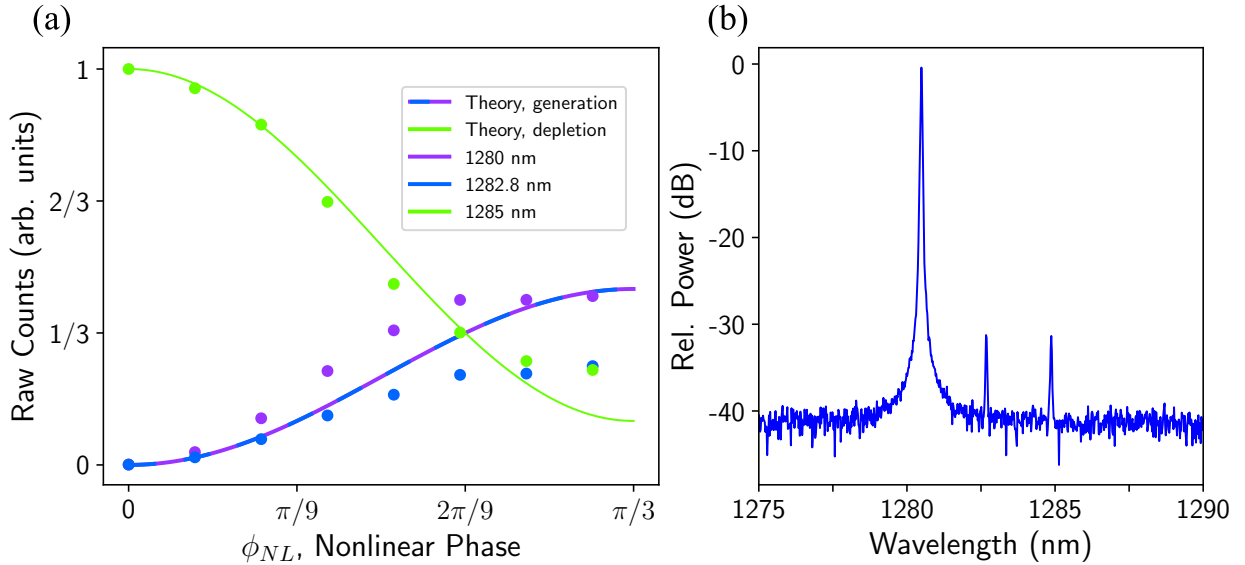


Figure 5: Raw singles rates as a function of power, normalized to input signal rate at zero pump power.

Since the depletion curve (the rates measured for the input frequency as it is converted to the other two wavelengths) can be normalized to 1 at zero pump power, only one free parameter is needed to convert the horizontal scale from the pump peak power to the nonlinear phase. To determine the horizontal scale, we fit the normalized depletion curve to the analytical curve (under the above ideal assumptions). The peak pump power of the three pumps, measured directly from oscilloscope traces for each data point, can then be converted to nonlinear phase. This in turn fixes the nonlinear phase for all three curves.

As the two generation curves start at zero counts at zero nonlinear phase, they cannot be normalized in the same way as the depletion curve without assuming the absolute rate at some nonzero nonlinear phase. This would entail an impractical measurement of the individual losses for each channel following the nonlinear fiber, which is unreliable due to the dependence of the freespace filters and detectors on polarization. The polarization changes frequently as it is optimized during each run of the experiment. Rather than attempt to correct for these losses directly, we use the fact that the loss is fixed for a given channel throughout the experiment, meaning that there is a single loss factor for each depletion curve. To obtain this factor, we perform a least-squares fit to the corresponding theory curves using the previously determined nonlinear phase, resulting in Fig. 3 of the main text. Note that, as derived earlier, the presence of propagation loss changes only the vertical and horizontal scale but not the shape of the curves; furthermore, using the propagation loss of 0.43 dB/km at 1285 nm provided by Corning for our Vistacor fiber, these scales deviate from the true scales by $< 1\%$.

In the classical regime (where the mean photon number is 10s of decibels higher than the latching limit of the SNSPDs), we readily verify that the two generation curves are in fact symmetric by sending the output of the nonlinear fiber directly into an optical spectrum analyzer (OSA). While filtering the individual channels inevitably introduces asymmetric losses, the OSA can measure a full spectrum with uniform insertion losses. The spectrum in Fig. 3 of the main text strongly verifies the symmetric distribution of power in the three channels after accounting for the duty cycle of the input signal. Further deviations from theory in Fig. 3 of main text are mostly due to the departure from the assumptions of zero phase mismatch and equal pump powers.

4.2 Dual-Frequency Input

To generate the coincidence curves of Fig. 4 (main text), for both classical and quantum coincidence measurements we follow a similar procedure as for the single-frequency input case. The raw coincidence curves are first normalized by the concurrent accidental rates at zero power, that is, the product of the corresponding singles rates taken at a time window at fixed relative delay with respect to the pump pulses such that the pumps are off. This quantity may be written

$$R_{\text{coinc}} = \frac{\langle \hat{a}_3^\dagger \hat{a}_1^\dagger \hat{a}_1 \hat{a}_3 \rangle}{\langle \hat{a}_1^\dagger \hat{a}_1 \rangle_0 \langle \hat{a}_3^\dagger \hat{a}_3 \rangle_0}, \quad (\text{S78})$$

where the 0-subscript in $\langle \cdot \rangle_0$ denotes the quantity in the absence of Bragg scattering, at zero pump power. This quantity is proportional to the integrated second-order correlation function. To complete the normalization such that the coincidence curve is equal to 1 at zero nonlinear phase, for all data points we normalize with respect to this same quantity at zero nonlinear phase. Finally, the conversion factor from relative pump pulse power to nonlinear phase is set by fitting the normalized, respective *singles* curves to the analytical curves, using the independently-measured pre-fiber losses and multiphoton parameters for the case of photon-pair input.

References

- [1] Govind P. Agrawal. Chapter 2 - pulse propagation in fibers. In Govind P. Agrawal, editor, *Nonlinear Fiber Optics (Sixth Edition)*, pages 27–55. Academic Press, sixth edition edition, 2019.
- [2] C. J. McKinstrie, J. D. Harvey, S. Radic, and M. G. Raymer. Translation of quantum states by four-wave mixing in fibers. *Opt. Express*, 13(22):9131–9142, Oct 2005.
- [3] Alessandro Farsi. *Coherent Manipulation Of Light In The Classical And Quantum Regimes Via Four-Wave Mixing Bragg Scattering*. PhD thesis, Cornell University, 2015.
- [4] Chaitali Joshi. *Frequency Domain Quantum Processing via Four-Wave Mixing*. PhD thesis, Cornell University, 2020.
- [5] Robert W. Boyd. Chapter 2 - Wave-Equation Description of Nonlinear Optical Interactions. In *Nonlinear Optics (Third Edition)*, pages 69–133. Academic Press, Burlington, third edition edition, 2008.

- [6] N. Quesada, L. G. Helt, M. Menotti, M. Liscidini, and J. E. Sipe. Beyond photon pairs—nonlinear quantum photonics in the high-gain regime: a tutorial. *Adv. Opt. Photon.*, 14(3):291–403, Sep 2022.
- [7] Zhe-Yu Jeff Ou. *Quantum States of Multi-Mode Fields*, chapter Chapter 4, pages 107–128. World Scientific, 2017.